



HAL
open science

Conditions of chondrule formation in ordinary chondrites

Maxime Piralla, Johan Villeneuve, Valentina Batanova, Emmanuel Jacquet,
Yves Marrocchi

► **To cite this version:**

Maxime Piralla, Johan Villeneuve, Valentina Batanova, Emmanuel Jacquet, Yves Marrocchi. Conditions of chondrule formation in ordinary chondrites. *Geochimica et Cosmochimica Acta*, 2021, 313, pp.295-312. 10.1016/j.gca.2021.08.007 . hal-03368913

HAL Id: hal-03368913

<https://hal.science/hal-03368913>

Submitted on 7 Oct 2021

HAL is a multi-disciplinary open access archive for the deposit and dissemination of scientific research documents, whether they are published or not. The documents may come from teaching and research institutions in France or abroad, or from public or private research centers.

L'archive ouverte pluridisciplinaire **HAL**, est destinée au dépôt et à la diffusion de documents scientifiques de niveau recherche, publiés ou non, émanant des établissements d'enseignement et de recherche français ou étrangers, des laboratoires publics ou privés.

Conditions of chondrule formation in ordinary chondrites

Maxime Piralla^{1,*}, Johan Villeneuve¹, Valentina Batanova², Emmanuel Jacquet³ &
Yves Marrocchi¹

¹*Université de Lorraine, CNRS, CRPG, UMR 7358, Vandœuvre-lès-Nancy 54500, France*

²*Université Grenoble Alpes, ISTERre, CNRS, UMR 5275, Grenoble 38000, France*

³*Institut de Minéralogie, de Physique des Matériaux et de Cosmochimie (IMPMC), Muséum
national d'Histoire naturelle, Sorbonne Université, CNRS, UMR 7590, CP52, 57 rue Cuvier,
Paris 75005, France*

**Corresponding author: maxime.piralla@univ-lorraine.fr*

Keywords: ordinary chondrites, chondrules, oxygen isotopes, gas-melt interactions, inner
protoplanetary disk

Unified Astronomy Thesaurus: Chondrites (228), Chondrules (229), Isotopic abundances
(867), Protoplanetary disks (1300)

23 **Abstract**

24 Chondrules are sub-millimetric spheroids that are ubiquitous in chondrites and
25 whose formation mechanism remains elusive. Textural and oxygen isotopic characteristics of
26 chondrules in carbonaceous chondrites (CCs) suggest that they result from the recycling of
27 isotopically heterogeneous early-condensed precursors via gas-melt interactions. Here, we
28 report high-resolution X-ray elemental maps and *in situ* O isotopic analyses of FeO-poor,
29 olivine-rich chondrules from ordinary chondrites (OCs) to compare the conditions of
30 chondrule formation in these two main classes of chondrites. OC chondrules show minor
31 element (e.g., Ti, Al) zonings at both the chondrule and individual olivine grain scales.
32 Considering the entire isotopic data set, our data define a mass-independent correlation,
33 with olivine grains showing O isotopic variations spanning more than 40 ‰. Though ¹⁶O-rich
34 relict olivine grains were identified in OC chondrules, they are much less abundant than in
35 CC chondrules. They appear as two types: (i) those with low minor element abundances and
36 $\Delta^{17}\text{O} < -15$ ‰ and (ii) those with varying minor element abundances and less negative $\Delta^{17}\text{O}$
37 values averaging -5.5 ‰. The host olivine grains exhibit mass-dependent O isotopic
38 variations within individual chondrules.

39 Our results reveal that similar processes (precursor recycling and interactions
40 between chondrule melts and a SiO- and Mg-rich gas) established the observed features of
41 OC and CC chondrules. The mass-dependent isotopic variations recorded by host olivine
42 grains result from kinetic effects induced by complex evaporation/recondensation processes
43 during the gas-melt interactions. This suggests that OC chondrules formed through
44 enhanced recycling processes, in good agreement with the lower abundances of relict
45 olivine grains in OC chondrules compared to CC chondrules. We use the $\Delta^{18}\text{O} = \delta^{18}\text{O} - \delta^{17}\text{O}$
46 parameter to demonstrate that there is no genetic relationship between CC and OC

47 chondrules, suggesting limited radial transport in the protoplanetary disk. Finally, to the first
48 order, the $\Delta^{18}\text{O}-\Delta^{17}\text{O}$ diagram may allow the non-carbonaceous vs. carbonaceous origin of a
49 given chondrule to be deciphered.

50 **1- Introduction**

51

52 Whether primitive or differentiated, meteorites exhibit a fundamental isotopic
53 dichotomy between a carbonaceous (C) and a non-carbonaceous (NC) superclan (Trinquier
54 et al., 2009; Warren, 2011; Budde et al., 2016; Kruijer et al., 2017, 2020; Nanne et al., 2019;
55 Burkhardt et al., 2019; Kleine et al., 2020). Compared to their NC counterparts, C meteorites
56 are enriched in neutron-rich isotopes of many elements with different geochemical and
57 cosmochemical behaviors (e.g., Ti, Cr, Ni) thus representing a fundamental characteristic of
58 the solar system (Kleine et al., 2020). Combined with the chronology of iron meteorites, the
59 NC–C dichotomy suggests that meteorites derived from two genetically distinct reservoirs
60 that coexisted but remained spatially separated between 1 and ~3–4 Myr after the
61 formation of Ca-Al-rich inclusions (CAIs), the oldest known solids in the solar system (Kruijer
62 et al., 2017; Desch et al., 2018; Kleine et al., 2020). This prolonged physical barrier between
63 the two reservoirs remains a matter of debate, and may reflect the early formation of
64 Jupiter (Kruijer et al., 2017), a pressure maximum in the disk (Brasser and Mojzsis, 2020), or
65 the preponderant role of the snowline (Lichtenberg et al., 2021). We note that the
66 subsequent loss of any intermediate materials also remains a possibility (Jacquet et al.,
67 2019). Regardless of their origins, the NC and C reservoirs are considered to represent the
68 primordial inner and outer parts of the solar system, respectively (Trinquier et al., 2007;
69 Warren, 2011; Kruijer et al., 2017, 2020; Desch et al., 2018; Burkhardt et al., 2019).

70 The isotopic dichotomy observed among bulk chondrites has now also been observed
71 at the scale of individual chondrules (Schneider et al., 2020), sub-millimetric igneous silicate
72 spheroids formed during the evolution of the protoplanetary disk (Connolly and Jones,
73 2016). NC chondrules have bulk oxygen, ^{50}Ti , and ^{54}Cr isotopic compositions uniformly

74 similar to their host chondrites, whereas chondrules in carbonaceous chondrites (CCs) have
75 more variable compositions, sometimes differing from that of their host chondrite (Williams
76 et al., 2020; Schneider et al., 2020). Although the isotopic compositions of CC and NC
77 chondrules may overlap for individual isotope ratios, this does not hold in multi-isotope
78 space, i.e., (i) no CC chondrule plots within the field of NC chondrites (although a few plot
79 near NC achondrites; Williams et al. 2020) and (ii) no NC chondrule plots within the field of
80 CC chondrites (Schneider et al., 2020). Consistent with transport simulations by Goldberg et
81 al. (2015), these characteristics suggest that chondrules essentially accreted where they had
82 formed, with a predominant effect of their precursor heterogeneity (Gerber et al., 2017;
83 Schneider et al., 2020) as opposed to large-scale (that is, reaching across C and NC reservoir
84 boundaries) chondrule transport in the disk after their formation (van Kooten et al., 2016;
85 Williams et al., 2020). That is, the varied isotopic compositions of CC chondrules may result
86 from the mixing of NC dust with a chemically variable dust component having a CAI- or
87 amoeboid olivine aggregate (AOA)-like isotopic composition (Schneider et al., 2020).
88 Conversely, the narrow range of nucleosynthetic anomalies observed in NC chondrules
89 suggests that they formed from different precursors and/or under different conditions.
90 Therefore, this dichotomy ultimately calls into question the conditions of dust formation in
91 the NC and CC reservoirs.

92 Type I (i.e. FeO-poor), CC chondrules are characterized by the frequent presence of
93 relict olivine grains that are generally more ^{16}O -rich than their host olivines (e.g., Jones et al.,
94 2004; Rudraswami et al., 2011; Ushikubo et al., 2012; Tenner et al., 2013, 2015, 2018;
95 Schrader et al., 2018, 2020; Hertwig et al., 2018; Chaumard et al., 2018, 2021; Marrocchi et
96 al., 2018, 2019a; Schneider et al., 2020; Ushikubo and Kimura, 2021; Weisberg et al., 2021).
97 Relict olivine grains are interpreted as chondrule precursor minerals that survived the high-

98 temperature chondrule forming event(s) (Jones et al., 2004). Recent high-current X-ray maps
99 and secondary ion mass spectrometry (SIMS) measurements of relict olivine grains have
100 revealed that they are characterized by low refractory element (Al, Ti) contents, similar to
101 those observed in olivine grains within AOAs (Jacquet and Marrocchi, 2017; Marrocchi et al.,
102 2018, 2019a). It has thus been proposed that type I chondrules are derived from AOAs or
103 AOA-related nebular materials; these nebular condensates underwent partial melting and
104 subsequent interactions with SiO- and Mg-rich gas (Marrocchi et al., 2018, 2019a; Villeneuve
105 et al., 2020; Jacquet et al., 2021; Jacquet, 2021).

106 Relict olivine grains are also observed in chondrules from ordinary chondrites (OCs,
107 the most abundant type of NC chondrites), but in lower abundances than in CC chondrules
108 (Kita et al., 2010; Tenner et al., 2018; Marrocchi et al., 2019a; Schrader et al., 2020). It has
109 been proposed that ¹⁶O-rich relict olivine grains within OC chondrules originated from the C
110 reservoir (Kita et al., 2010), but this is difficult to reconcile with the spatially and chemically
111 distinct NC and C reservoirs inferred from nucleosynthetic anomalies (Gerber et al., 2017;
112 Spitzer et al., 2020; Schneider et al., 2020). Still, the similar O isotopic compositions of CAIs
113 in non-carbonaceous and carbonaceous chondrites (e.g., McKeegan et al. 1998; Guan et al.
114 2000; Fagan et al. 2001) must suggest common descent for part of their components.

115 The oxygen isotope systematics of OC chondrules themselves also differ from those
116 of their CC chondrule counterparts. They exhibit more ^{17,18}O-rich isotopic compositions (i.e.,
117 $\Delta^{17}\text{O} \approx 0\text{--}1\text{ ‰}$; Kita et al., 2010) than CC chondrules ($-5\text{ to }-2\text{ ‰}$; Tenner et al., 2013, 2015,
118 2018; Schrader et al., 2014, 2020; Hertwig et al., 2018; Chaumard et al., 2018, 2021;
119 Marrocchi et al., 2018, 2019a; Jabeen et al., 2019) and show internal mass-dependent
120 fractionations not yet observed in CC chondrules (Kita et al., 2010; Schrader et al., 2014,
121 2018, 2020; Tenner et al., 2018; Marrocchi et al., 2018, 2019a). Within OCs, type I

122 porphyritic olivine (PO) chondrules tend to have lower $\delta^{18}\text{O}$ values than type I porphyritic
123 pyroxene (PP) chondrules with similar $\Delta^{17}\text{O}$ values (Kita et al., 2010). This characteristic has
124 been ascribed to either kinetic isotopic fractionations during multiple evaporation events or
125 equilibrium isotopic partitioning between molten chondrule precursors and a CO-H₂O-rich
126 gas of varying composition (Kita et al., 2010). However, the textural similarity between OC
127 and CC chondrules (Libourel and Portail, 2018; Marrocchi et al., 2018, 2019a; Jacquet et al.,
128 2021) may indicate comparable interactions between the melts and SiO- and Mg-rich gas.

129 To better understand the conditions of type I chondrule formation in the NC
130 reservoir, we selected type I PO chondrules from the pristine ordinary chondrites Semarkona
131 (LL3.00), Piancaldoli (LL3.10), and Bishunpur (LL3.15; Grossman and Brearley, 2005;
132 Marrocchi et al., 2020). We report a comprehensive study of chondrule olivine grains
133 combining petrological observations and quantitative geochemical analyses. We use our
134 results to discuss (i) the nature and conditions of the chondrule-forming events in the NC
135 reservoir based on textural and O isotopic evidence, (ii) how they compare with those in the
136 C reservoir, and (iii) implications for dynamics within the protoplanetary disk.

137

138 **2- Materials & Methods**

139

140 *2-1- Samples*

141

142 We surveyed all chondrules within (i) a home-made thick section of Piancaldoli (3.10;
143 Marrocchi et al., 2020) and (ii) thick sections from the Muséum national d'Histoire naturelle
144 (Paris, France) of Semarkona (LL3.00, section 3583; Grossman and Brearley, 2005) and
145 Bishunpur (LL3.15, section 2491sp4; Grossman and Brearley, 2005). We selected 11 type I

146 PO chondrules for further analyses: one from Semarkona, six from Piancaldoli, and four from
147 Bishunpur.

148

149 *2-2- Elemental mapping and analyses*

150

151 High-resolution cathodoluminescence (CL), elemental X-ray mapping, and
152 quantitative point analyses were performed at the Institut des Sciences de la Terre (ISTerre,
153 Grenoble, France) using a JEOL JXA 8230 electron microprobe equipped with five
154 wavelength-dispersive spectrometers (WDS), silicon drift detector energy-dispersive
155 spectrometer (SDD-EDS; Batanova et al., 2015), and panchromatic cathodoluminescence
156 system. High-resolution CL maps coupled with fast major element (Mg, Fe, Si) X-ray maps
157 (on WDS detectors) were acquired simultaneously using an acceleration voltage of 20 kV, a
158 beam current of 100 nA, 1.5-2 μm step size, and a dwell time of 10 ms. This allows the
159 identification of olivine, pyroxene, and glass in chondrules. High-resolution elemental X-ray
160 maps were performed with an acceleration voltage of 20 kV and a beam current of 500 nA;
161 the step size and dwell time were set to 1.5–2 μm and 330–600 ms, respectively, to achieve
162 acquisition times of 18–24 h depending on map size. Al, Ca, Cr, Mn, and Ti were measured
163 by WDS and Mg, Fe, and Si by EDS. Detection limits were below 40 ppm for Al, Ca, Ti, Cr, and
164 Mn as estimated from the minimum differences between the average concentrations of
165 visually distinct homogeneous zones and the standard deviations of the concentrations
166 within homogeneous zones. These X-ray maps are semi-quantitative, because the
167 backgrounds were not quantified in similar off-peak maps. Quantitative analyses of Al, Ti, Ca,
168 Cr, Mn, Ni, Mg, Fe, and Si in all olivine grains large enough to be isotopically characterized by
169 SIMS were performed with an accelerating voltage of 20 kV, probe current of 900 nA, beam

170 diameter of 1 μm (diameter of interaction volume around 5 μm). The total peak/background
171 counting time was 400 s for Al, Ti, Ca, Mn and 200 s for Cr and Ni with equal counting time in
172 positions of peak and background measured from both side of the peak (e.g., Batanova et
173 al., 2018). Such a high current and long counting times allow very low detection limits, here
174 estimated to be about 10 ppm for Al, Ca, and Ti, and below 20 ppm for Cr, Mn, and Ni
175 (Batanova et al. 2015; 2018). Mg, Fe, and Si were simultaneously measured on the EDS
176 detector. The JEOL software ZAF method was used for matrix corrections. MongOL sh11-2
177 olivine reference material (Batanova et al., 2019) was used for major element
178 standardization and for monitoring analytical accuracy and precision during measurements.

179

180 *2-3- Isotopic analyses*

181

182 We measured the oxygen isotopic compositions of type I chondrule olivine grains by
183 SIMS, targeting nearly all olivine grains within each chondrule, and performed multiple
184 analyses within the coarsest zoned olivine grains. We used the CAMECA IMS 1270 E7 at the
185 Centre de Recherches Pétrographiques et Géochimiques (CRPG-CNRS, Nancy, France). $^{16}\text{O}^-$,
186 $^{17}\text{O}^-$, and $^{18}\text{O}^-$ ions produced by a Cs^+ primary ion beam ($\sim 10 \mu\text{m}$, $\sim 2\text{--}2.5 \text{ nA}$, rastered over 5
187 $\times 5 \mu\text{m}^2$) were measured in multi-collection mode using three Faraday cups (FCs). To remove
188 the $^{16}\text{OH}^-$ interference on the $^{17}\text{O}^-$ peak and to maximize the flatness atop the $^{16}\text{O}^-$ and $^{18}\text{O}^-$
189 peaks, the entrance and exit slits of the central FC were adjusted to obtain mass resolution
190 power ($\text{MRP} = M/\Delta M$) of $\sim 7,000$ for $^{17}\text{O}^-$. The two off-axis multicollection FCs, L'2 and H1,
191 were respectively used to measure $^{16}\text{O}^-$ and $^{18}\text{O}^-$ and were set on exit slit 1 ($\text{MRP} = 2,500$).
192 We used $10^{10} \Omega$, $10^{12} \Omega$, and $10^{11} \Omega$ resistors for the L'2 (^{16}O), central (^{17}O), and H1 (^{18}O) FCs,
193 respectively (see Bouden et al., 2021 for further details). As an additional safeguard against

194 $^{16}\text{OH}^-$ interference, a liquid N_2 trap was used to reduce the pressure in the analysis chamber
195 to $<1 \times 10^{-8}$ mbar. A normal-incidence electron gun was used for charge compensation. Total
196 measurement times were 300 s, comprising 120 s of pre-sputtering and 180 s of analysis.
197 Two terrestrial standards, San Carlos olivine and JV1 diopside, were used to define the mass-
198 dependent fractionation line. The instrumental mass fractionation (IMF) of chondrule olivine
199 grains was corrected using San Carlos olivine. To monitor any instrumental drift and to
200 achieve good precision, the San Carlos olivine was analyzed after every 15–20 sample
201 analyses. Typical count rates obtained on San Carlos olivine were 1.0×10^9 cps, 4.0×10^5 cps,
202 and 2.1×10^6 cps for ^{16}O , ^{17}O , and ^{18}O , respectively. All SIMS analytical spots were checked
203 thoroughly by scanning electron microscope, and any spots near fractures, in the mesostasis,
204 or not completely within olivine grains were excluded from the dataset. Isotopic
205 compositions are reported in delta notation relative to Vienna standard mean ocean water
206 (V-SMOW) as $\delta^{17,18}\text{O} = (^{17,18}\text{O}/^{16}\text{O})_{\text{Sample}} / (^{17,18}\text{O}/^{16}\text{O})_{\text{V-SMOW}} - 1$ (expressed in ‰). Typical 2σ
207 measurement errors, accounting for internal errors on each measurement and the external
208 reproducibility of the standards, were estimated to be ~ 0.4 ‰ for $\delta^{18}\text{O}$, ~ 0.7 ‰ for $\delta^{17}\text{O}$, and
209 ~ 0.7 ‰ for $\Delta^{17}\text{O} = \delta^{17}\text{O} - 0.52 \times \delta^{18}\text{O}$ (representing mass-independent deviation from the
210 terrestrial fractionation line, TFL).

211

212 **3- Results**

213

214 The selected type I PO chondrules range from 150 to 700 μm in diameter. They
215 comprise rounded to euhedral olivine crystals with variable sizes; olivines are mostly <50 μm
216 in the inner parts of chondrules and are generally larger subhedral to euhedral grains in the
217 outer parts (Figs. 1–3, Figs. S1–S8). Five chondrules show large dusty olivine grains (Figs. 2–3,

218 Figs. S3–S4, S8) and a 0.5-mm-long olivine macrocryst was observed in the Piancaldoli Ch-6
219 chondrule (Fig. S4). Chondrule rims are dominated by low-Ca pyroxenes oriented parallel to
220 the chondrule surface and containing resorbed or poikilitically enclosed olivine grains (Figs.
221 1–3, Figs. S1–S8). A few metal beads with variable sizes up to 100 μm were observed in the
222 mesostasis with no clear preferential locations within the chondrules.

223 Chondrule olivine grains appear homogeneous in back-scattered electron images
224 (Figs. 1–3, Figs. S2–S8) and have homogenous major element compositions ($\text{Mg\#} =$
225 $94.3\text{--}99.5$, where $\text{Mg\#} = \text{Mg}/(\text{Mg} + \text{Fe})$ in mol%; Figs. 1–3, Figs. S1–S8, Table S1), but high-
226 current X-ray maps reveal complex chemical zonings at both the chondrule and olivine scales
227 (Figs. 1–3, Figs. S2–S8, Table S1). Olivine grains in the inner parts of chondrules show Al-, Ti-,
228 Mn-, and Cr-depleted cores surrounded by overgrowths enriched in these trace or minor
229 elements (Figs. 1–3, Figs. S2–S8, Table S1). Similar zonings are also observed perpendicular
230 to the long axes of olivine bars in the Semarkona Ch-4 chondrule (Fig. S8), similar to
231 observations by Libourel and Portail (2018). Dusty olivine grains areas are uniformly Ca-, Al-,
232 and Ti-poor and Mn-rich and, in Bishunpur Ch-6, are accompanied by oscillatory-zoned
233 hopper textured crystals (Fig. 3). Olivine grains in the outer parts of chondrules are
234 characterized by asymmetric trace and minor element distributions: closer to the chondrule
235 center, olivine compositions are similar to those in interior chondrule olivines, and toward
236 the outer edge of chondrules, Ca, Al, and Ti contents increase then decrease again, whereas
237 Mn, Cr, and Fe contents increase monotonically (Figs. 1–3, Figs. S2–S8, Table S1). Olivine
238 minor and trace element concentrations range from 30 to 1,500 ppm TiO_2 , 100 to 9,700 ppm
239 Al_2O_3 , 970 to 9,700 ppm CaO, 50 to 4,600 ppm MnO, 800 to 10,000 ppm Cr_2O_3 , and 15 to
240 3,600 ppm NiO (Figs. 1–3, Figs. S2–S8, Table S1). These zonings are comparable to those
241 observed in carbonaceous chondrites (Marrocchi et al., 2018, 2019a).

242 Across the entire dataset, olivine O isotopic compositions vary widely, with $\delta^{18}\text{O}$ and
243 $\delta^{17}\text{O}$ values ranging respectively from -40.9‰ to $+9.0\text{‰}$ and from -44.0‰ to $+6.5\text{‰}$ (Fig.
244 4). Our data define a good correlation with $\delta^{17}\text{O} = [0.97 \pm 0.02] \times \delta^{18}\text{O} - [1.0 \pm 0.9]\text{‰}$
245 (MSWD = 4.7, $r^2 = 0.94$, $n = 649$). As in our previous works (Marrocchi et al., 2018, 2019a),
246 we adopt the convention of Ushikubo et al. (2012) and consider olivine grains with $\Delta^{17}\text{O}$
247 values beyond 3σ (analytical error) from that of their host olivine to be relicts. This is a
248 conservative approach. For example, the standard deviation on the $\Delta^{17}\text{O}$ value of the “host
249 olivine” in chondrule Bishunpur Ch-2 is twice the analytical error (Table S3), and the
250 $\delta^{18}\text{O}$ - $\Delta^{17}\text{O}$ plot suggests a bimodal distribution of $\Delta^{17}\text{O}$ values around 1 and 2 ‰ (Fig. S9);
251 therefore, there are likely “hidden” relict olivine beyond the three ^{16}O -rich (i.e., below the
252 TFL in Fig. S9) ones recognized in this chondrule.

253 Host olivine grains have $\delta^{18}\text{O}$ and $\delta^{17}\text{O}$ values ranging from -4.0‰ to $+9.0\text{‰}$, with
254 $\Delta^{17}\text{O}$ values between -2.6 and $+3.6\text{‰}$. It is to note that the chondrule Piancaldoli Ch-8 has a
255 mean $\Delta^{17}\text{O} = -1.8 \pm 0.7\text{‰}$ distinct from the other with a mean $\Delta^{17}\text{O} = +0.9 \pm 1.3\text{‰}$ (Fig. 4,
256 Tables S1, S3). The mean host $\delta^{18}\text{O}$ value (including Piancaldoli Ch-8) is 3.6‰ , somewhat
257 higher than the value of 1.9‰ reported for type I PO chondrules by Kita et al. (2010) but
258 comparable to that of their type I POP chondrules (3.9‰). The average intra-chondrule
259 standard deviation of host olivine $\delta^{18}\text{O}$ values is 1.0‰ , regardless of the presence or
260 absence of relicts (Fig. 5A–B, Tables S1, S3); this value is higher than the value of 0.3‰
261 reported for type I PO or POP chondrules by Kita et al. (2010), but similar to the value of 1.1
262 ‰ reported for carbonaceous chondrites by Marrocchi et al. (2018, 2019a). The highest $\delta^{18}\text{O}$
263 (i.e., isotopically heaviest) host olivine values seem restricted to analyses in chondrule
264 interiors (Fig. 6).

265 Of our 649 oxygen isotopic measurements, only 17, or about 3%, correspond to relict
266 olivine grains according to the threshold of Ushikubo et al. (2012), much lower than the 17 %
267 and 10 % reported for the carbonaceous chondrites NWA 5958 (C2-ung) and Kaba (CV3) by
268 Marrocchi et al. (2018, 2019a). This is consistent with previous literature data: Hertwig et al.
269 (2018) reported 24 % of analyzed olivines in Kaba (CV3) to be relicts and Chaumard et al.
270 (2018) reported 14 % in Murchison (CM2), whereas Kita et al. (2010) reported 7 % in LL
271 chondrites. However, direct comparison of the absolute percentages may be hampered by
272 the different search strategies because the few analyses per chondrule in past literature
273 studies (usually $n = 2-10$; e.g., Kita et al., 2010; Rudraswami et al., 2011; Hertwig et al., 2018;
274 Chaumard et al., 2018; Tenner et al., 2018) may have been biased in favor of large host
275 olivine crystals. Relict olivine grains do not show any specific spatial distributions within
276 chondrules. They also have narrower ranges of Ti, Al, and Cr contents and Mg# than their
277 host olivine grains and are depleted in Ni and Mn (Fig. 7; Tables S1–S3). Of note, relict olivine
278 grains with $\Delta^{17}\text{O} < -15\text{‰}$ are systematically depleted in all these elements except Cr (Fig. 7,
279 Tables S1–S3). Relict grains plot roughly along the Primary Chondrule Minerals (PCM) line
280 defined by Ushikubo et al. (2012) for the carbonaceous chondrite Acfer 094, but, like our
281 host grains, seem systematically shifted toward its left (Fig. 4). This can be quantified by the
282 mass-fractionation parameter $\Delta^{18}\text{O} = \delta^{18}\text{O} - \delta^{17}\text{O}$ (e.g., Zanda et al., 2006; Figs. 8, S10),
283 which corresponds to the delta of the $^{18}\text{O}/^{17}\text{O}$ ratio and is thus insensitive to ^{16}O
284 enrichments or depletions. $\Delta^{18}\text{O}$ is on average 2.1 ‰ in relict olivines ($n = 17$ grains, 1 SD =
285 0.9 ‰; Figs. 8, S10, Table S2) and 1.1 ‰ in host olivines ($n = 11$ chondrule averages, 1 SD =
286 0.5 ‰; Figs. 8, S10, Table S3); these values are somewhat higher than the average of 0.45 ‰
287 obtained for type I PO chondrules by Kita et al. (2010). In terms of this parameter, the PCM
288 corresponds to $\Delta^{18}\text{O} = 2.7 \text{‰}$ (strictly speaking, $[0.013 \pm 0.013] \times \delta^{18}\text{O} + [2.7 \pm 0.11] \text{‰}$ using

289 the parameterization of Ushikubo et al., 2012), consistent with our previous data on relict
290 and host grains in carbonaceous chondrites (Marrocchi et al., 2018, 2019a; Fig. 8). Such
291 displaced $\Delta^{18}\text{O}$ values in OC relict grains are also apparent in analyses of dusty grains
292 (Schrader et al., 2020) and the ^{16}O -rich olivines of Baeza Bravo (2019), although one cannot
293 unequivocally distinguish between relicts and ^{16}O -rich hosts in the latter study because of
294 the low number of analyses per chondrule.

295

296 **4- Discussion**

297

298 *4-1 Origin of chondrule textures*

299

300 In CCs, type I PO chondrules are characterized by complex chemical zonings at the
301 scales of both chondrules and individual olivine grains (Libourel and Portail, 2018; Marrocchi
302 et al., 2018, 2019a), with inner-chondrule olivine grains showing Al-, Ti-, Mn-, and Cr-
303 depleted cores surrounded by overgrowths enriched in those elements. At chondrule
304 margins, olivine grains exhibit asymmetric grain growths and distributions of trace and minor
305 elements, with Ca, Al, and Ti contents increasing and then decreasing toward the outer
306 chondrule edge (Marrocchi et al., 2018, 2019a). Our results show similar features for OC
307 chondrules with (i) chemically zoned trace and minor element contents (e.g., Al, Ti, Mn, and
308 Cr; Figs. 1–3, S2–S8; Table S1) and (ii) the asymmetric growth of outer-chondrule crystals
309 (Figs. 1–3, S1–S8). However, we also observed more complex textures such as hopper-
310 textured olivine crystals in porphyritic OC chondrules (e.g., Fig. 3), which, in CCs, have only
311 been reported in barred olivine chondrules (Libourel and Portail, 2018).

312 Elements such as Cr might be mobilized during low-grade metamorphism (Grossman
313 and Brearley, 2005). However, Cr in type II FeO-rich olivine grains is not affected in
314 Semarkona (Grossman and Brearley, 2005) nor in Piancaldoli (Marrocchi et al., 2020) but
315 could be modified in Bishunpur (Grossman and Brearley, 2005). Similarly, metamorphism
316 can slightly affect the Cr distribution in Mg-rich olivine grains of Bishunpur. For the other
317 elements, Ca could be affected due to its relatively fast diffusion within Mg-rich olivine but Ti
318 and Al are not affected as their respective diffusion rates in Mg-rich olivine are very slow
319 (e.g., Chakraborty, 2010), as may be judged from the preserved fine structure of the zoning.
320 The observed zonings thus appear inherited from the (pre-accretionary) chondrule-forming
321 processes.

322 Overall, the similarity of the features observed in OC and CC chondrules indicates
323 that these processes were essentially the same at different heliocentric distances in the
324 protoplanetary disk: (i) the melting of precursor aggregates containing isotopically diverse
325 (and sometimes AOA-like) materials produced, owing to partial evaporation, refractory Ca-
326 Al-Ti-rich melt; (ii) crystallization of Ca-Al-Ti-rich host olivines from the melt around
327 preserved Al-Ti-poor relicts; and (iii) the subsequent crystallization of Ca-Al-Ti-poor olivine,
328 especially on outer-chondrule rims, was enhanced by the recondensation of Mg and SiO
329 (also diluting the aforementioned refractory incompatible elements), which eventually also
330 promoted pyroxene crystallization (Libourel and Portail, 2018; Marrocchi et al., 2018, 2019a;
331 Villeneuve et al., 2020; Jacquet et al., 2021). Interactions with the surrounding gases would
332 have rapidly buffered the O isotopic composition of the melt to that of the local reservoir,
333 which explains the limited variability of host olivine $\Delta^{17}\text{O}$ values beyond analytical error. The
334 surrounding gases included SiO and likely also H₂O (Ushikubo et al., 2012; Schrader et al.,
335 2013, 2014; Tenner et al., 2013, 2015; Hertwig et al., 2018; Chaumard et al., 2018), which

336 may have isotopically exchanged O with the melt and/or contributed to the net influx of O
337 through reactions such as $\text{SiO}_{(g)} + \text{H}_2\text{O}_{(g)} = \text{SiO}_2(l) + \text{H}_2(g)$.

338

339 *4-2 Mass-dependent oxygen isotopic variations*

340

341 Host olivine $\delta^{18}\text{O}$ and $\delta^{17}\text{O}$ values range from -4.0‰ to $+9.0\text{‰}$ and from -3.5‰ to
342 $+6.5\text{‰}$, respectively (Figs. 4, S10, Table S1). Interestingly, they define a correlation ($\delta^{17}\text{O} =$
343 $[0.76 \pm 0.06] \times \delta^{18}\text{O} - [0.08 \pm 0.14] \text{‰}$; MSWD = 0.21, $r^2 = 0.80$, $n = 632$) whose slope is
344 shallower than that of the entire data set (0.97 ± 0.02 ; see section 3) but steeper than 0.52.
345 However, taken separately, the host olivine gains in individual chondrules plot along
346 particular mass fractionation (i.e., slope 0.52) lines (e.g., Bishunpur Ch-6, Fig. 5A). This
347 implies that the intermediate slope observed in the combined host olivine data set results
348 from the various $\Delta^{17}\text{O}$ values of the individual chondrules (Figs. 8, S10, Table S3). Finally, the
349 intra-chondrule ranges of host olivine $\delta^{18}\text{O}$ values vary from 1.7 to 13 ‰ (with intra-
350 chondrule host olivine 1 SD of 0.5 – 1.9 ‰; Table S3), with the largest intra-chondrule
351 variations being comparable to the range of the entire host olivine dataset.

352 In this subsection, we investigate the origin of these isotopic variations. We first note
353 that oxygen diffuses very slowly in solid olivine (e.g., diffusivities below $10^{-17} \text{ m}^2/\text{s}$,
354 corresponding to $\sim 1 \mu\text{m}^2/\text{d}$, below 1600 °C; e.g., Chakraborty, 2010), such that each olivine
355 spot should preserve the O isotopic composition it had upon crystallization. Although such
356 isotopic variations might be explained by melt-crystal isotopic fractionations, the observed
357 variations are larger than those predicted under equilibrium crystallization (e.g., $\ln(\alpha_{\text{olivine-}}$
358 $\text{basaltic melt}) \approx \delta^{18}\text{O}_{\text{olivine}} - \delta^{18}\text{O}_{\text{basaltic melt}} < 1\text{‰}$; Eiler, 2001; Zhao and Zheng, 2003). Another
359 possibility is kinetic fractionations induced by diffusion and growth reactions (Tiller et al.,

1953; Smith et al., 1955; Albarede and Bottinga, 1972). Specifically, a boundary layer that has become depleted or enriched in some element via crystallization may induce diffusive transport of that element in the melt, and thus isotopic fractionation if the diffusivity depends on isotopologue mass. Such a process could generate isotopic fractionations as large as $\sim 10\text{‰}$ for $\delta^{18}\text{O}$ (Jambon, 1980; Watkins et al., 2017), of similar magnitude to those observed within OC chondrules. (Figs. 4, 5; Tables S1, S3). However, we exclude this process for several reasons. First, the fast crystallization of large crystals ($>0.5\text{ cm}$) is required to produce such extended isotopic fractionations, whereas all chondrule olivine grains are smaller than $200\text{ }\mu\text{m}$ (excluding the large olivine crystal in chondrule Ch-6 of Piancaldoli; Fig. S4). Second, the power law dependence on isotope mass used by Jambon (1980) is rather high for natural condensed systems (Leshner, 2010; Watkins et al., 2017). Third, convective (isotopically insensitive) transport must be negligible, which Jambon (1980) deemed unlikely for viscosities below $10^5\text{ Pa}\cdot\text{s}$, an upper limit for typical high-temperature chondrule melts (e.g., Gooding and Keil, 1981). Finally, the theoretical analytical model is only developed for 1D systems, whereas numerical 3D simulations tend to show reduced fractionations (Watson and Müller, 2009; Watkins et al., 2017). Therefore, the large, kinetic, and mass-dependent isotopic variations observed within OC chondrules cannot have resulted from chemical and isotopic disequilibrium during crystallization from chondrule melts, and olivine crystals should essentially record the isotopic composition of their immediate parental melt.

The large observed O isotopic variations could also be related to gas-melt interactions during chondrule formation. Although a single O-bearing molecule is often considered in isotopic models of chondrule formation (i.e., only $\text{H}_2\text{O}_{(\text{g})}$ or $\text{SiO}_{(\text{g})}$), several major O-bearing molecules co-existed, whether considering (i) a high-temperature gas of solar composition (Larimer, 1967; Lodders, 2003; Javoy et al., 2012), (ii) a dust-enriched

384 region subject to evaporation (Ebel and Grossman, 2000), or (iii) impact-generated vapor
385 plumes (Visscher and Fegley, 2013). Equilibrium fractionations between the main O-bearing
386 species at temperatures of 500–1573 K (i.e., $\text{SiO}_{(g)}$, $\text{H}_2\text{O}_{(g)}$, and $\text{CO}_{(g)}$; Richet et al., 1977; Javoy
387 et al., 2012) would predict $\delta^{18}\text{O}$ values increasing in the order olivine $\approx \text{SiO}_{(g)} < \text{H}_2\text{O}_{(g)} < \text{CO}_{(g)}$
388 (with the last being about 3 ‰ higher than the first at the highest temperatures; e.g. Javoy
389 et al., 2012). Consequently, olivine should be isotopically lighter than the nebular gas. This
390 would account for the low average $\Delta^{18}\text{O}$ values of the olivine hosts (1.1 ‰) compared to the
391 whole-rock chondrites (1.53 and 1.89 ‰ for Piancaldoli and Bishunpur, respectively; Zanda
392 et al., 2006; Marrocchi et al., 2020). With varying temperature, changing fractionation
393 factors and condensate/gas ratios would yield only minor isotopic variations in olivine, <2 ‰
394 for $\delta^{18}\text{O}$, even allowing for fractional condensation (Kita et al., 2010), and thus cannot be
395 responsible for most of the observed intra-chondrule variations. We note in passing that our
396 type I PO chondrules are isotopically comparable to Kita et al.'s (2010) type I POP and PP
397 chondrules but at odds with the lighter isotopic compositions of their type I PO chondrules,
398 which they ascribed to higher equilibration temperatures.

399 Considering gas-melt interactions, the oxygen isotopic compositions of chondrule
400 precursors may have differed from that of the surrounding gas, and molten chondrules
401 would have evolved toward equilibrium. This would imply that host olivine grains that
402 crystallized at various stages of the gas-melt isotopic exchange (by continual condensation
403 and evaporation) record that isotopic evolution, and thus varying $\Delta^{17}\text{O}$ and/or $\Delta^{18}\text{O}$ values.
404 However, this is not consistent with the uniform $\Delta^{17}\text{O}$ values obtained for host olivine grains
405 (within analytical errors). One could, of course, conceive that the endmembers of this
406 putative mixing lay along a slope 0.52 line (i.e., constant $\Delta^{17}\text{O}$) in the oxygen three-isotope
407 plot, but relict grains (which would be representative of the solid precursors) are generally

408 displaced from their hosts (closer to the gas-solid average) roughly along a line of slope 1
409 (e.g., Figs. 4, 5B, 8, S10). Consequently, any evidence of an initial isotopic disequilibrium
410 must have been lost when the host olivines started to crystallize.

411 However, even if the ambient gas and chondrule melts were at *isotopic* equilibrium,
412 *chemical* disequilibrium could have induced isotopic variations via the net transfer of oxygen
413 from one phase to another. This would tend to temporarily enrich the latter phase in light O-
414 isotopes because, at a given temperature, lighter isotopologues move faster from one phase
415 to another than their heavier counterparts (e.g., Richter et al., 2002; Fig. 9). Importantly,
416 such isotopic fractionations would have been mass-dependent and thus would have not
417 affected the $\Delta^{17}\text{O}$ value, as observed in OC chondrules (Fig. S10).

418 In more detail, oxygen would suffer a net evaporation during the initial heating of
419 chondrule precursors, inducing the preferential loss of light isotopes to the undersaturated
420 gas (Fig. 9). Assuming that evaporation coefficients are not mass-dependent, the
421 evaporating SiO may have presented a fractionation relative to the source melt down to
422 $[M(\text{Si}^{16}\text{O})/M(\text{Si}^{18}\text{O})]^{1/2} - 1 = -22 \text{ ‰}$ for $\delta^{18}\text{O}$ (e.g., Richter et al., 2002). Via this mechanism,
423 the melt could have attained the isotopically heaviest compositions observed in host olivine
424 grains after a few tens of percent of evaporation. As that olivine would have started
425 crystallizing after the evaporation stage, the earliest host olivine to crystallize would have
426 been isotopically heavy. These early-crystallized host olivine grains would have formed the
427 immediate overgrowths of relict crystals in chondrule interiors, which may explain why the
428 heaviest compositions are observed in some interior grains (Fig. 9). The fact that these
429 compositions are not clearly spatially systematic may reflect various degrees of overlap of
430 SIMS analytical spots with relict grains (not necessarily manifest in $\Delta^{17}\text{O}$; e.g., Bishunpur Ch-
431 2) or the outermost (later-crystallized) parts of the overgrowths.

432 Upon cooling, the preferential condensation of light isotopes from the oversaturated
433 gas would gradually shift the melt isotopic compositions toward lighter values, as recorded
434 by the successively crystallized olivine. Of note, the melt composition might even
435 temporarily become isotopically lighter than the equilibrium prediction before converging
436 back toward it as the oversaturation of gaseous species eventually decreased (Fig. 9). The
437 intensity and record of these isotopic variations during host olivine crystallization would
438 depend on the exact thermal history, which might have been more complicated than a single
439 heating and cooling stage. Our isotopic data show $\Delta^{18}\text{O}$ values (extending to negative values)
440 beyond equilibrium fractionation predictions from an isotopically homogeneous bulk OC-like
441 reservoir (Fig. S10), implying that the range of isotopic compositions within each individual
442 chondrule was set by these kinetic effects.

443

444 *4-3 OC chondrule precursors and their relationship to the CC reservoir*

445

446 It is well known that most OC chondrules have $\Delta^{17}\text{O}$ values higher than most of their
447 CC counterparts (e.g., Kita et al., 2010; Tenner et al., 2018; Figs. 8, S10), possibly due to
448 protracted gas-melt interactions during or before the chondrule-forming event(s) (e.g.,
449 Marrocchi et al., 2019a). Combined with literature data, our results reveal that OC
450 chondrules also have lower $\Delta^{18}\text{O}$ values than CC chondrules (Figs. 8, S10). Besides, the
451 average difference between the host olivine $\Delta^{18}\text{O}$ values in OC (1.1 ± 0.5 ‰, 1 SD) and CC
452 chondrules (3.4 ± 0.5 ‰, 1 SD; Marrocchi et al., 2018, 2019a) is consistent with the average
453 difference between those of the bulk chondrules (OCs, 1.4 ± 0.4 ‰; CCs, 3.5 ± 0.5 ‰, 1 SD;
454 Clayton et al., 1983, 1991; Clayton and Mayeda, 1985, 1999; Mayeda et al., 1988; Rubin et
455 al., 1990; Weisberg et al., 1993; Jones et al., 2004). Furthermore, CC chondrules show intra-

456 chondrule mass fractionations (1 SD = 1.1 ‰ for $\delta^{18}\text{O}$; Marrocchi et al., 2018, 2019a) similar
457 to those observed in OC chondrules (1 SD = 1 ‰ for $\delta^{18}\text{O}$; Table S3; see section 3), although
458 the former was not previously noticed due to the larger mass-independent variations
459 observed in CC chondrules. This suggests that the kinetic effects during host olivine
460 crystallization discussed in the preceding section, regardless of their causes, occurred with
461 similar magnitudes in both chondrite classes, in good agreement with their textural
462 similarities. However, the observed difference between the $\Delta^{18}\text{O}$ values of CC and OC
463 chondrules (~2 ‰) is larger than those produced during the chondrule-forming events
464 themselves (intra- and inter-chondrule $\Delta^{18}\text{O}$ SD = ~0.7 ‰ and ~0.5 ‰, respectively, in both
465 OCs and CCs; Figs. 8, S10, Table S3), indicating that OC chondrules cannot be derived from
466 the CC reservoir by kinetic effects attending one chondrule-forming event. Interestingly, in
467 OC chondrules, low $\Delta^{18}\text{O}$ values are observed for (i) both relict and host olivine grains (Figs.
468 8, S10, Tables S1-S3) and (ii) chondrules with negative $\Delta^{17}\text{O}$ values (e.g., Piancaldoli Ch8; Figs.
469 8, 10; Tables S1-S3). These low $\Delta^{18}\text{O}$ values in OC chondrules are also similar to those of their
470 host chondrites, with the average bulk OC $\Delta^{18}\text{O}$ value being 1.6 ‰, compared to 3.8 ‰ for
471 CO chondrites (Zanda et al., 2006). This suggests that the different O isotopic compositions
472 of the OC and CC reservoirs were already established before the final chondrule-forming
473 events.

474 Two distinct types of relict grains occur in OC chondrules: (i) those with low trace
475 element contents, $\Delta^{17}\text{O} < -15$ ‰, and $\Delta^{18}\text{O}$ values similar to those of CC relict and host
476 olivine grains and (ii) those with varying trace element contents, $\Delta^{17}\text{O} \approx -5.5$ ‰, and $\Delta^{18}\text{O}$
477 values lower than those of CC relict and host olivine grains (Figs. 7, 8). Interestingly, the
478 former (or at least the two found in this study) have chemical and isotopic features similar to
479 CC relicts', which characteristics have been interpreted as inherited from nebular

480 condensates similar to AOAs (Marrocchi et al., 2018, 2019a; Villeneuve et al., 2020; see Fig.
481 8, S10). This thus suggests a genetic link between early condensates and chondrules in both
482 the OC and CC reservoirs. Conversely, OC relicts with $\Delta^{17}\text{O} \approx -5.5 \text{‰}$, although having similar
483 $\Delta^{17}\text{O}$ and minor element contents than CC host olivine grains, show significantly different
484 $\Delta^{18}\text{O}$ values compared to CC relict and host olivine grains (Fig. 8). This indicates that even the
485 ^{16}O -rich materials in OCs are not dominated by a contribution from the CC reservoir,
486 consistent with the limited mixing between C and NC reservoirs inferred from the O-Cr-Ti
487 systematics of NC and CC chondrules (Schneider et al., 2020). This is also consistent with the
488 paucity of refractory inclusions in OCs (usually $\ll 0.1 \text{ vol } \%$, e.g., Kimura et al., 2002,
489 compared to 1–13 vol % in CV, CO, and CM chondrites, e.g., Krot et al., 2014), which limits
490 the contribution of CC material in OCs to less than $\sim 1 \text{ %}$ in order of magnitude (not to
491 mention the possibility that part of the refractory inclusions may have never been through a
492 C reservoir, if they were dispersed throughout the disk before the C/NC dichotomy came
493 into being). The type (ii) relicts could result from extensive recycling of previous chondrule
494 generations, as suggested by the high chondrule fraction in OCs (Figs. 10–11).

495 To quantitatively estimate this process, we refer to the Marrocchi et al. (2019a)
496 chondrule recycling calculation and assume that (i) the different chondrule-forming events
497 experienced by a given grain of nebular matter were independent and rare, and (ii) the
498 chondrule/matrix ratio of an OC is representative of the chondrule/dust ratio of the
499 reservoir from which it formed. Considering the modal chondrule abundances of 81 and 84
500 % in Piancaldoli and Semarkona, respectively (Zanda et al., 2006; Marrocchi et al., 2020), the
501 model of Marrocchi et al. (2019a) would then imply that ~ 61 and 66 % of chondrule matter
502 had been recycled from previous chondrule-forming events. In this framework, the higher
503 the modal abundance of chondrules, the higher the amount of chondrule reprocessing.

504 Interestingly, the $\Delta^{18}\text{O}-\Delta^{17}\text{O}$ trend could be related to the abundance of chondrules in the
505 different types of chondrites, with relatively chondrule-rich chondrites showing lower $\Delta^{18}\text{O}$
506 values (Figs. 8, 10). Then, the intermediate position in the $\Delta^{18}\text{O}-\Delta^{17}\text{O}$ diagram of OC relicts
507 [type (ii)] with $\Delta^{17}\text{O} \approx -5.5 \text{ ‰}$ and $\Delta^{18}\text{O} \approx 2.1 \text{ ‰}$ may record previous steps of chondrule
508 recycling if they indeed represent the debris of earlier generations of chondrules. That is,
509 although a single chondrule-forming event may not have produced sufficient mass
510 fractionation to account for the presently observed shift of the chondrule hosts from the
511 PCM, the cumulative effect of several such episodes may have (e.g., by some distillation
512 process in which the isotopically heavy gas was lost after each episode). Such a high degree
513 of OC chondrule reprocessing may explain the low abundance of isotopically identifiable
514 relict olivine grains, in particular those from pre-chondrule (AOA-like) precursors [the type (i)
515 of the previous paragraph], compared to CCs. This thus attests to the higher efficiency of
516 transient thermal events in the inner solar system. Our results thus demonstrate the
517 predominant role of gas-melt interactions under different conditions in the inner and outer
518 solar system in generating the petrographic and isotopic features of OC and CC chondrules
519 (Fig. 11).

520 Although OCs and CCs show different $\Delta^{18}\text{O}$ values (Figs. 8, 10, S10, S11), they form a
521 continuum trend from the low $\Delta^{17}\text{O}$ and high $\Delta^{18}\text{O}$ values of CK- and CM-related chondrites
522 (e.g., NWA 5958) to high $\Delta^{17}\text{O}$ and low $\Delta^{18}\text{O}$ values of OC chondrites (Fig. 10, S11). This
523 continuum contrasts with the gaps reported in other isotopic biplots (e.g., tracing inherited
524 presolar components) used to discuss the NC-C dichotomy (Warren, 2011; Kruijer et al.,
525 2017, 2020; Nanne et al., 2019; Burkhardt et al., 2019; Kleine et al., 2020). That said, $\Delta^{18}\text{O}$
526 values may still be used to a first order to constrain the NC or C origin of a given
527 chondrule/grain as both chondritic superclans are well-resolved in the $\Delta^{18}\text{O}-\Delta^{17}\text{O}$ diagram

528 (Figs. 8, 10, S11). We note that although import from CC into the NC reservoir seems quite
529 small, evidence for isotopically NC-like chondrules in CV and CK chondrites (Williams et al.
530 2020) and OC-like dusty olivine relicts in CM chondrules (Schrader et al. 2020) suggests more
531 important, if limited, transport in the other direction, from NC to CC.

532

533 **5- Concluding remarks**

534

535 We performed high-resolution elemental X-ray mapping analyses coupled with *in situ*
536 O isotopic measurements of most of the visible olivine grains from 11 chondrules in the
537 Bishunpur, Piancaldoli, and Semarkona ordinary chondrites. Our main results are:

538 1- OC olivine-rich chondrules are characterized by complex chemical zonings at both the
539 chondrule and grain scales. Inner-chondrule olivine grains have Al-, Ti-, Mn-, and Cr-depleted
540 cores surrounded by overgrowths enriched in those elements, whereas outer-chondrule
541 olivines grew asymmetrically and are depleted in refractory elements toward the chondrule
542 edges.

543 2- All olivine grains define a good correlation with $\delta^{17}\text{O} = [0.97 \pm 0.02] \times \delta^{18}\text{O} - [1.0 \pm 0.9] \text{‰}$
544 (MSWD = 4.7, $r^2 = 0.94$, $n = 649$). Host olivines define another correlation with a shallower
545 slope: $\delta^{17}\text{O} = [0.76 \pm 0.06] \times \delta^{18}\text{O} - [0.08 \pm 0.14] \text{‰}$ (MSWD = 0.21, $r^2 = 0.80$, $n = 632$).

546 3- Relict olivine grains, if identified as having $\Delta^{17}\text{O}$ values beyond 3σ of those of their host
547 grains, represent only 3 % of the analyzed olivines. This abundance is lower than that
548 reported in CC chondrules (~10–20 %). Two types of relicts were observed: (i) those with
549 extreme ^{16}O enrichments ($\Delta^{17}\text{O} < -15 \text{‰}$) and low Al_2O_3 and TiO_2 concentrations and (ii)
550 those with moderately negative $\Delta^{17}\text{O}$ values around -5.5‰ and variable minor element
551 abundances.

552 From these data, we drew the following conclusions:

553 1. The similar features observed in OC and CC chondrules indicate that chondrule formation
554 processes were essentially the same within different reservoirs of the protoplanetary disk.

555 The melting of precursor aggregates containing isotopically diverse material produced
556 refractory Ca-Al-Ti-rich melts from which host olivine grains crystallized around preserved Al-
557 Ti-poor relicts. The subsequent crystallization of Ca-Al-Ti-poor olivine grains, especially at the
558 outer edges of chondrules, resulted from the recondensation of Mg- and SiO-rich gas.

559 2- Host olivine grains in both OC and CC chondrules show intra-chondrule mass-dependent
560 variations along lines of slope 0.52, with 1 SD \approx 1 ‰ for $\delta^{18}\text{O}$. In CC chondrules, these
561 variations were not previously noticed because of the larger mass-independent variations
562 shown by relict grains commonly measured in CC chondrules.

563 3- These mass-dependent intra-chondrule isotopic variations can only be explained by
564 kinetic effects during gas-melt interactions, and result from evaporation and recondensation
565 during chondrule formation.

566 4- The distinct $\Delta^{18}\text{O}$ ($= \delta^{18}\text{O} - \delta^{17}\text{O}$) and $\Delta^{17}\text{O}$ values observed in OC and CC chondrules at
567 both the bulk chondrule and individual grain (host and relict) scales indicate that the OC and
568 CC reservoirs were already separated before the final chondrule-forming events.

569 5- Among relict grains, those with extreme ^{16}O -enrichments ($\Delta^{17}\text{O} < -15$ ‰) and low Al_2O_3
570 and TiO_2 concentrations share similarities with AOA olivine grains, indicating a genetic link
571 between early-condensed refractory inclusions and chondrules. Although the other relict
572 grains with $\Delta^{17}\text{O} \approx -5.5$ ‰ and variable trace element abundances share similarities with CC
573 host olivine grains, their distinct $\Delta^{18}\text{O}$ values imply that they do not result from the recycling
574 of CC chondrules. Instead, this supports a local origin for OC chondrules, which resulted from
575 several episodes of chondrule formation.

576 6- The $\Delta^{18}\text{O}-\Delta^{17}\text{O}$ trend appears to be controlled by the abundance of chondrules, which
577 might result from cumulative effects over several chondrule-forming events. The enhanced
578 recycling of OC chondrules resulted in lower abundances of relict grains compared to CC
579 chondrules.

580 7- Although the $\Delta^{18}\text{O}-\Delta^{17}\text{O}$ trend displays an isotopic continuum unlike the real gaps
581 observed in other isotopic biplots featuring the NC-C dichotomy, the $\Delta^{18}\text{O}$ parameter can be
582 used, to a first order, to decipher the NC vs. C origin of a given chondrule.

583

584

585 **Acknowledgments**

586

587 Nordine Bouden is thanked for technical assistance with SIMS measurements. We are
588 grateful to the Muséum national d'Histoire naturelle of Paris for loaning the Bishunpur and
589 Semarkona samples. Tim Fagan, Arshad Ali and an anonymous reviewer are thanked for
590 constructive comments and Associate Editor Yuri Amelin for careful editing. This research
591 was founded by l'Agence Nationale de la Recherche (ANR) through grant CASSYSS ANR-18-
592 CE31-0010-01 (PI Johan Villeneuve). This is CRPG contribution #2771.

593

594 **Research Data**

595 Original data from this study are available on the Ordar database:
596 <https://doi.org/10.24396/ORDAR-69>

597

598 **References**

- 599 Albarede F. and Bottinga Y. (1972) Kinetic disequilibrium in trace element partitioning
600 between phenocrysts and host lava. *Geochimica et Cosmochimica Acta* **36**, 141–156.
- 601 Baeza Bravo L. I. (2019) Oxygen isotope systematics of ordinary chondrite chondrules:
602 insights into the inner solar system planetary reservoir. *Master's thesis*. Australian
603 National University.
- 604 Batanova V. G., Sobolev A. V. and Kuzmin D. V. (2015) Trace element analysis of olivine: High
605 precision analytical method for JEOL JXA-8230 electron probe microanalyser. *Chemical*
606 *Geology* **419**, 149–157.
- 607 Batanova, V. G., Sobolev, A. V. & Magnin, V. (2018). Trace element analysis by EPMA in
608 geosciences: detection limit, precision and accuracy. Emas 2017 Workshop - 15th
609 European Workshop on Modern Developments and Applications in Microbeam
610 Analysis & Iumas-7 Meeting - 7th Meeting of the International Union of Microbeam
611 Analysis Societies. Bristol: *Iop Publishing Ltd*, v 304.
- 612 Batanova V. G., Thompson J. M., Danyushevsky L. V., Portnyagin M. V., Garbe-Schönberg D.,
613 Hauri E., Kimura J., Chang Q., Senda R., Goemann K., Chauvel C., Campillo S., Ionov D.
614 A. and Sobolev A. V. (2019) New Olivine Reference Material for *In Situ* Microanalysis.
615 *Geostand Geoanal Res* **43**, 453–473.
- 616 Bouden N., Villeneuve J., Marrocchi Y., Deloule E., Füri E., Gurenko A., Piani L., Thomassot E.,
617 Peres P. and Fernandes F. (2021) Triple Oxygen Isotope Measurements by Multi-
618 Collector Secondary Ion Mass Spectrometry. *Front. Earth Sci.* **8**, 601169.
- 619 Brasser R. and Mojzsis S. J. (2020) The partitioning of the inner and outer Solar System by a
620 structured protoplanetary disk. *Nature Astronomy* **4**, 492–499.
- 621 Budde G., Burkhardt C., Brennecka G. A., Fischer-Gödde M., Kruijer T. S. and Kleine T. (2016)
622 Molybdenum isotopic evidence for the origin of chondrules and a distinct genetic
623 heritage of carbonaceous and non-carbonaceous meteorites. *Earth and Planetary*
624 *Science Letters* **454**, 293–303.
- 625 Burkhardt C., Dauphas N., Hans U., Bourdon B. and Kleine T. (2019) Elemental and isotopic
626 variability in solar system materials by mixing and processing of primordial disk
627 reservoirs. *Geochimica et Cosmochimica Acta* **261**, 145–170.
- 628 Chakraborty S. (2010) Diffusion Coefficients in Olivine, Wadsleyite and Ringwoodite. *Reviews*
629 *in Mineralogy and Geochemistry* **72**, 603–639.
- 630 Chaumard N., Defouilloy C., Hertwig A. T. and Kita N. T. (2021) Oxygen isotope systematics of
631 chondrules in the Paris CM2 chondrite: Indication for a single large formation region
632 across snow line. *Geochimica et Cosmochimica Acta* **299**, 199–218.
- 633 Chaumard N., Defouilloy C. and Kita N. T. (2018) Oxygen isotope systematics of chondrules in
634 the Murchison CM2 chondrite and implications for the CO-CM relationship.
635 *Geochimica et Cosmochimica Acta* **228**, 220–242.
- 636 Clayton R. N., Mayeda T., Hutcheon I., Molini-Velsko C., Onuma N., Ikeda Y. and Olsen E.
637 (1983) Oxygen isotopic compositions of chondrules in Allende and ordinary chondrites.
638 In *Chondrules and their origins* pp. 37–43.

- 639 Clayton R. N. and Mayeda T. K. (1999) Oxygen isotope studies of carbonaceous chondrites.
640 *Geochimica et Cosmochimica Acta* **63**, 2089–2104.
- 641 Clayton R. N. and Mayeda T. K. (1985) Oxygen isotopes in chondrules from enstatite
642 chondrites: Possible identification of a major nebular reservoir. In *Sixteenth lunar and*
643 *planetary science conference Lunar and Planetary Institute*, Houston. Abstract #1072.
- 644 Clayton R. N., Mayeda T. K., Goswami J. N. and Olsen E. J. (1991) Oxygen isotope studies of
645 ordinary chondrites. *Geochimica et Cosmochimica Acta* **55**, 2317–2337.
- 646 Connolly H. C. and Jones R. H. (2016) Chondrules: The canonical and noncanonical views: A
647 Review of Chondrule Formation. *J. Geophys. Res. Planets* **121**, 1885–1899.
- 648 Desch S. J., Kalyaan A. and Alexander C. M. O'D. (2018) The Effect of Jupiter's Formation on
649 the Distribution of Refractory Elements and Inclusions in Meteorites. *ApJS* **238**, 11.
- 650 Ebel D. S. and Grossman L. (2000) Condensation in dust-enriched systems. *Geochimica et*
651 *Cosmochimica Acta* **64**, 339–366.
- 652 Eiler J. M. (2001) Oxygen Isotope Variations of Basaltic Lavas and Upper Mantle Rocks.
653 *Reviews in Mineralogy and Geochemistry* **43**, 319–364.
- 654 Fagan T. J., McKeegan K. D., Krot A. N. and Keil K. (2001) Calcium-aluminum-rich inclusions in
655 enstatite chondrites (II): Oxygen isotopes. *Meteorit Planet Sci* **36**, 223–230.
- 656 Fukuda K., Brownlee D. E., Joswiak D. J., Tenner T. J., Kimura M. and Kita N. T. (2021)
657 Correlated isotopic and chemical evidence for condensation origins of olivine in comet
658 81P/Wild 2 and in AOAs from CV and CO chondrites. *Geochimica et Cosmochimica Acta*
659 **293**, 544–574.
- 660 Gerber S., Burkhardt C., Budde G., Metzler K. and Kleine T. (2017) Mixing and Transport of
661 Dust in the Early Solar Nebula as Inferred from Titanium Isotope Variations among
662 Chondrules. *Astrophys J* **841**, L17.
- 663 Goldberg A. Z., Owen J. E. and Jacquet E. (2015) Chondrule transport in protoplanetary discs.
664 *Mon. Not. R. Astron. Soc.* **452**, 4054–4069.
- 665 Gooding J. L. and Keil K. (1981) Estimated viscosities and implied thermal histories of
666 chondrule droplets. In *Twelfth lunar and planetary science conference Lunar and*
667 *Planetary Institute*, Houston. Abstract #1124.
- 668 Grossman J. N. and Brearley A. J. (2005) The onset of metamorphism in ordinary and
669 carbonaceous chondrites. *Meteorit Planet Sci* **40**, 87–122.
- 670 Guan Y., McKeegan K. D. and MacPherson G. J. (2000) Oxygen isotopes in calcium–
671 aluminum-rich inclusions from enstatite chondrites: new evidence for a single CAI
672 source in the solar nebula. *Earth and Planetary Science Letters* **181**, 271–277.
- 673 Hertwig A. T., Defouilloy C. and Kita N. T. (2018) Formation of chondrules in a moderately
674 high dust enriched disk: Evidence from oxygen isotopes of chondrules from the Kaba
675 CV3 chondrite. *Geochimica et Cosmochimica Acta* **224**, 116–131.
- 676 Jabeen I., Kusakabe M., Nagao K. and Ali A. (2019) Oxygen isotope signatures in bulk
677 chondrules: Implications for the aqueous alteration and thermal metamorphism on the
678 Allende CV3 parent body. *Meteorit Planet Sci* **54**, 431–451.

- 679 Jacquet E. (2021) Collisions and compositional variability in chondrule-forming events.
680 *Geochimica et Cosmochimica Acta* **296**, 18–37.
- 681 Jacquet E., Alard O. and Gounelle M. (2015) Trace element geochemistry of ordinary
682 chondrite chondrules: The type I/type II chondrule dichotomy. *Geochimica et*
683 *Cosmochimica Acta* **155**, 47–67.
- 684 Jacquet E. and Marrocchi Y. (2017) Chondrule heritage and thermal histories from trace
685 element and oxygen isotope analyses of chondrules and amoeboid olivine aggregates.
686 *Meteorit Planet Sci* **52**, 2672–2694.
- 687 Jacquet E., Pignatale F. C., Chaussidon M. and Charnoz S. (2019) Fingerprints of the
688 Protosolar Cloud Collapse in the Solar System. II. Nucleosynthetic Anomalies in
689 Meteorites. *Astrophys J* **884**, 32.
- 690 Jacquet E., Piralla M., Kersaho P. and Marrocchi Y. (2021) Origin of isolated olivine grains in
691 carbonaceous chondrites. *Meteorit Planet Sci* **56**, 13–33.
- 692 Jambon A. (1980) Isotopic fractionation: A kinetic model for crystals growing from magmatic
693 melts. *Geochimica et Cosmochimica Acta* **44**, 1373–1380.
- 694 Javoy M., Balan E., Méheut M., Blanchard M. and Lazzeri M. (2012) First-principles
695 investigation of equilibrium isotopic fractionation of O- and Si-isotopes between
696 refractory solids and gases in the solar nebula. *Earth and Planetary Science Letters*
697 **319–320**, 118–127.
- 698 Jones R. H., Leshin L. A., Guan Y., Sharp Z. D., Durakiewicz T. and Schilk A. J. (2004) Oxygen
699 isotope heterogeneity in chondrules from the Mokoia CV3 carbonaceous chondrite.
700 *Geochimica et Cosmochimica Acta* **68**, 3423–3438.
- 701 Kimura M., Hiyagon H., Palme H., Spettel B., Wolf D., Clayton R. N., Mayeda T. K., Sato T.,
702 Suzuki A. and Kojima H. (2002) Yamato 792947, 793408 and 82038: The most primitive
703 H chondrites, with abundant refractory inclusions. *Meteorit Planet Sci* **37**, 1417–1434.
- 704 Kita N. T., Nagahara H., Tachibana S., Tomomura S., Spicuzza M. J., Fournelle J. H. and Valley
705 J. W. (2010) High precision SIMS oxygen three isotope study of chondrules in LL3
706 chondrites: Role of ambient gas during chondrule formation. *Geochimica et*
707 *Cosmochimica Acta* **74**, 6610–6635.
- 708 Kleine T., Budde G., Burkhardt C., Kruijer T. S., Worsham E. A., Morbidelli A. and Nimmo F.
709 (2020) The Non-carbonaceous–Carbonaceous Meteorite Dichotomy. *Space Sci Rev*
710 **216**, 55.
- 711 Krot A. N., Keil K., Scott E. R. D., Goodrich C. A. and Weisberg M. K. (2014) Classification of
712 Meteorites and Their Genetic Relationships. In *Treatise on Geochemistry* (eds. H. D.
713 Holland and K. K. Turekian). Elsevier, Oxford. pp. 1–63.
- 714 Krot A. N., Nagashima K., Fintor K. and Pál-Molnár E. (2019) Evidence for oxygen-isotope
715 exchange in refractory inclusions from Kaba (CV3.1) carbonaceous chondrite during
716 fluid-rock interaction on the CV parent asteroid. *Geochimica et Cosmochimica Acta*
717 **246**, 419–435.
- 718 Kruijer T. S., Burkhardt C., Budde G. and Kleine T. (2017) Age of Jupiter inferred from the
719 distinct genetics and formation times of meteorites. *Proc Natl Acad Sci USA*,
720 201704461.

- 721 Kruijer T. S., Kleine T. and Borg L. E. (2020) The great isotopic dichotomy of the early Solar
722 System. *Nature Astronomy* **4**, 32–40.
- 723 Larimer J. W. (1967) Chemical fractionations in meteorites—I. Condensation of the
724 elements. *Geochimica et Cosmochimica Acta* **31**, 1215–1238.
- 725 Leshner C. E. (2010) Self-diffusion in Silicate Melts: Theory, Observations and Applications to
726 Magmatic Systems. *Reviews in Mineralogy and Geochemistry* **72**, 269–309.
- 727 Libourel G. and Portail M. (2018) Chondrules as direct thermochemical sensors of solar
728 protoplanetary disk gas. *Sci. Adv.* **4**, eaar3321.
- 729 Lichtenberg T., Drążkowska J., Schönbächler M., Golabek G. J. and Hands T. O. (2021)
730 Bifurcation of planetary building blocks during Solar System formation. *Science* **371**,
731 365–370.
- 732 Lodders K. (2003) Solar System Abundances and Condensation Temperatures of the
733 Elements. *Astrophys J* **591**, 1220–1247.
- 734 Marrocchi Y., Bonal L., Gattacceca J., Piani L., Beck P., Greenwood R., Eschrig J., Basque A.,
735 Nuccio P. M. and Martin F. F. (2020) The Piancaldoli meteorite: A forgotten primitive
736 LL3.10 ordinary chondrite. *Meteorit Planet Sci* **55**, maps.13552.
- 737 Marrocchi Y., Euverte R., Villeneuve J., Batanova V., Welsch B., Ferrière L. and Jacquet E.
738 (2019a) Formation of CV chondrules by recycling of amoeboid olivine aggregate-like
739 precursors. *Geochimica et Cosmochimica Acta* **247**, 121–141.
- 740 Marrocchi Y., Villeneuve J., Jacquet E., Piralla M. and Chaussidon M. (2019b) Rapid
741 condensation of the first Solar System solids. *Proc Natl Acad Sci USA* **116**, 23461–
742 23466.
- 743 Marrocchi Y., Villeneuve J., Batanova V., Piani L. and Jacquet E. (2018) Oxygen isotopic
744 diversity of chondrule precursors and the nebular origin of chondrules. *Earth and
745 Planetary Science Letters* **496**, 132–141.
- 746 Mayeda T. K., Clayton R. N., Kring D. A. and Davis A. M. (1988) Oxygen, silicon, and
747 magnesium isotopes in ningqiang chondrules. *Meteoritics* **23**, 288.
- 748 McKeegan K. D., Leshin L. A., Russell S. S. and MacPherson G. J. (1998) Oxygen Isotopic
749 Abundances in Calcium- Aluminum-Rich Inclusions from Ordinary Chondrites:
750 Implications for Nebular Heterogeneity. *Science* **280**, 414–418.
- 751 Nanne J. A. M., Nimmo F., Cuzzi J. N. and Kleine T. (2019) Origin of the non-carbonaceous–
752 carbonaceous meteorite dichotomy. *Earth and Planetary Science Letters* **511**, 44–54.
- 753 Richet P., Bottinga Y. and Javoy M. (1977) A Review of Hydrogen, Carbon, Nitrogen, Oxygen,
754 Sulphur, and Chlorine Stable Isotope Fractionation Among Gaseous Molecules. *Annu.
755 Rev. Earth Planet. Sci.* **5**, 65–110.
- 756 Richter F. M., Davis A. M., Ebel D. S. and Hashimoto A. (2002) Elemental and isotopic
757 fractionation of Type B calcium-, aluminum-rich inclusions: experiments, theoretical
758 considerations, and constraints on their thermal evolution. *Geochimica et
759 Cosmochimica Acta* **66**, 521–540.

- 760 Rubin A. E., Wasson J. T., Clayton R. N. and Mayeda T. K. (1990) Oxygen isotopes in
761 chondrules and coarse-grained chondrule rims from the Allende meteorite. *Earth and*
762 *Planetary Science Letters* **96**, 247–255.
- 763 Rudraswami N. G., Ushikubo T., Nakashima D. and Kita N. T. (2011) Oxygen isotope
764 systematics of chondrules in the Allende CV3 chondrite: High precision ion microprobe
765 studies. *Geochimica et Cosmochimica Acta* **75**, 7596–7611.
- 766 Schneider J. M., Burkhardt C., Marrocchi Y., Brennecka G. A. and Kleine T. (2020) Early
767 evolution of the solar accretion disk inferred from Cr-Ti-O isotopes in individual
768 chondrules. *Earth and Planetary Science Letters* **551**, 116585.
- 769 Schrader D. L., Connolly H. C., Lauretta D. S., Nagashima K., Huss G. R., Davidson J. and
770 Domanik K. J. (2013) The formation and alteration of the Renazzo-like carbonaceous
771 chondrites II: Linking O-isotope composition and oxidation state of chondrule olivine.
772 *Geochimica et Cosmochimica Acta* **101**, 302–327.
- 773 Schrader D. L., Nagashima K., Davidson J., McCoy T. J., Oglione R. C. and Fu R. R. (2020)
774 Outward migration of chondrule fragments in the early Solar System: O-isotopic
775 evidence for rocky material crossing the Jupiter Gap? *Geochimica et Cosmochimica*
776 *Acta* **282**, 133–155.
- 777 Schrader D. L., Nagashima K., Krot A. N., Oglione R. C. and Hellebrand E. (2014) Variations in
778 the O-isotope composition of gas during the formation of chondrules from the CR
779 chondrites. *Geochimica et Cosmochimica Acta* **132**, 50–74.
- 780 Schrader D. L., Nagashima K., Waitukaitis S. R., Davidson J., McCoy T. J., Connolly H. C. and
781 Lauretta D. S. (2018) The retention of dust in protoplanetary disks: Evidence from
782 agglomeratic olivine chondrules from the outer Solar System. *Geochimica et*
783 *Cosmochimica Acta* **223**, 405–421.
- 784 Scott E. R. D. and Krot A. N. (2014) Chondrites and Their Components. In *Treatise on*
785 *Geochemistry* (eds. H. D. Holland and K. K. Turekian). Elsevier, Oxford. pp. 65–137.
- 786 Smith V. G., Tiller W. A. and Rutter J. W. (1955) A mathematical analysis of solute
787 redistribution during solidification. *Can. J. Phys.* **33**, 723–745.
- 788 Spitzer F., Burkhardt C., Budde G., Kruijer T. S., Morbidelli A. and Kleine T. (2020) Isotopic
789 Evolution of the Inner Solar System Inferred from Molybdenum Isotopes in Meteorites.
790 *Astrophys J* **898**, L2.
- 791 Tenner T. J., Nakashima D., Ushikubo T., Kita N. T. and Weisberg M. K. (2015) Oxygen isotope
792 ratios of FeO-poor chondrules in CR3 chondrites: Influence of dust enrichment and
793 H₂O during chondrule formation. *Geochimica et Cosmochimica Acta* **148**, 228–250.
- 794 Tenner T. J., Ushikubo T., Kurahashi E., Kita N. T. and Nagahara H. (2013) Oxygen isotope
795 systematics of chondrule phenocrysts from the CO3.0 chondrite Yamato 81020:
796 Evidence for two distinct oxygen isotope reservoirs. *Geochimica et Cosmochimica Acta*
797 **102**, 226–245.
- 798 Tenner T. J., Ushikubo T., Nakashima D., Schrader D. L., Weisberg M. K., Kimura M. and Kita
799 N. T. (2018) Oxygen Isotope Characteristics of Chondrules from Recent Studies by
800 Secondary Ion Mass Spectrometry. In *Chondrules* (eds. S. S. Russell, H. C. Connolly Jr.,
801 and A. N. Krot). Cambridge University Press. pp. 196–246.

- 802 Tiller W. A., Jackson K. A., Rutter J. W. and Chalmers B. (1953) The redistribution of solute
803 atoms during the solidification of metals. *Acta Metallurgica* **1**, 428–437.
- 804 Trinquier A., Birck J. and Allegre C. J. (2007) Widespread ⁵⁴Cr Heterogeneity in the Inner Solar
805 System. *Astrophys J* **655**, 1179–1185.
- 806 Trinquier A., Elliott T., Ulfbeck D., Coath C., Krot A. N. and Bizzarro M. (2009) Origin of
807 Nucleosynthetic Isotope Heterogeneity in the Solar Protoplanetary Disk. *Science* **324**,
808 374–376.
- 809 Ushikubo T. and Kimura M. (2021) Oxygen-isotope systematics of chondrules and olivine
810 fragments from Tagish Lake C2 chondrite: Implications of chondrule-forming regions in
811 protoplanetary disk. *Geochimica et Cosmochimica Acta* **293**, 328–343.
- 812 Ushikubo T., Kimura M., Kita N. T. and Valley J. W. (2012) Primordial oxygen isotope
813 reservoirs of the solar nebula recorded in chondrules in Acfer 094 carbonaceous
814 chondrite. *Geochimica et Cosmochimica Acta* **90**, 242–264.
- 815 van Kooten E. M. M. E., Wielandt D., Schiller M., Nagashima K., Thomen A., Larsen K. K.,
816 Olsen M. B., Nordlund Å., Krot A. N. and Bizzarro M. (2016) Isotopic evidence for
817 primordial molecular cloud material in metal-rich carbonaceous chondrites. *Proc Natl*
818 *Acad Sci USA* **113**, 2011–2016.
- 819 Villeneuve J., Marrocchi Y. and Jacquet E. (2020) Silicon isotopic compositions of chondrule
820 silicates in carbonaceous chondrites and the formation of primordial solids in the
821 accretion disk. *Earth and Planetary Science Letters* **542**, 116318.
- 822 Visscher C. and Fegley B. (2013) Chemistry of impact-generated silicate melt-vapor debris
823 disks. *Astrophys J* **767**, L12.
- 824 Warren P. H. (2011) Stable-isotopic anomalies and the accretionary assemblage of the Earth
825 and Mars: A subordinate role for carbonaceous chondrites. *Earth and Planetary*
826 *Science Letters* **311**, 93–100.
- 827 Watkins J. M., DePaolo D. J. and Watson E. B. (2017) Kinetic Fractionation of Non-Traditional
828 Stable Isotopes by Diffusion and Crystal Growth Reactions. *Reviews in Mineralogy and*
829 *Geochemistry* **82**, 85–125.
- 830 Watson E. B. and Müller T. (2009) Non-equilibrium isotopic and elemental fractionation
831 during diffusion-controlled crystal growth under static and dynamic conditions.
832 *Chemical Geology* **267**, 111–124.
- 833 Weisberg M. K., Kita N. T., Fukuda K., Siron G. and Ebel D. S. (2021) Micro-distribution of
834 oxygen isotopes in unequilibrated enstatite chondrites. *Geochimica et Cosmochimica*
835 *Acta* **300**, 279–295.
- 836 Weisberg M. K., Prinz M., Clayton R. N. and Mayeda T. K. (1993) The CR (Renazzo-type)
837 carbonaceous chondrite group and its implications. *Geochimica et Cosmochimica Acta*
838 **57**, 1567–1586.
- 839 Williams C. D., Sanborn M. E., Defouilloy C., Yin Q.-Z., Kita N. T., Ebel D. S., Yamakawa A. and
840 Yamashita K. (2020) Chondrules reveal large-scale outward transport of inner Solar
841 System materials in the protoplanetary disk. *Proc Natl Acad Sci USA* **117**, 23426–
842 23435.

- 843 Zanda B., Hewins R., Bourot Denise M., Bland P. and Albarede F. (2006) Formation of solar
844 nebula reservoirs by mixing chondritic components. *Earth and Planetary Science*
845 *Letters* **248**, 650–660.
- 846 Zhao Z.-F. and Zheng Y.-F. (2003) Calculation of oxygen isotope fractionation in magmatic
847 rocks. *Chemical Geology* **193**, 59–80.
- 848

849 **Figure Captions**

850

851 **Fig. 1.** (A) Back-scattered electron image of type I PO chondrule Ch-5 in LL3.15 Bishunpur
852 (section 2491sp4). Bright spots are metal beads. Black circular pits are previous LA-ICP-MS
853 analytical spots. (B) High-resolution TiO₂ X-ray map, revealing internal structures and
854 emphasizing that chondrules are radially zoned: the outer parts of chondrules contain Ti-rich
855 olivine grains and chondrule interiors are dominated by smaller, Ti-poor olivine grains
856 surrounded by mesostasis. Ti-rich overgrowths commonly mantle Ti-poor olivine cores. (C–F)
857 High-resolution Al₂O₃, CaO, MnO, and Cr₂O₃ X-ray maps, respectively. Color scales represent
858 the chemical composition of olivine grains; reddish colors indicate high abundances of minor
859 elements in other phases (e.g., mesostasis). Of note, this compound chondrule corresponds
860 to Bi30 in Jacquet et al. (2015) and Jacquet (2021).

861

862 **Fig. 2.** (A) Back-scattered electron image of type I PO chondrule Ch-2 in LL3.15 Bishunpur
863 (section 2491sp4). Black circular pits are previous LA-ICP-MS analytical spots. (B) False-color
864 X-ray composite map with Mg in red, Fe in green, and Si in blue; olivine appears in magenta,
865 pyroxene in purple, mesostasis in blue, and metal and sulfides in shades of green. (C)
866 Cathodoluminescence map revealing internal structures and emphasizing that chondrules
867 are radially zoned.

868

869 **Fig. 3.** (A) Back-scattered electron image of type I PO chondrule Ch-6 in LL3.15 Bishunpur
870 (section 2491sp4). Black circular pits are previous LA-ICP-MS analytical spots. (B–F) High-
871 resolution TiO₂, Al₂O₃, CaO, MnO, and Cr₂O₃ X-ray maps, respectively, as in Fig. 1. Of note,
872 this chondrule corresponds to Bi6 in Jacquet et al. (2015).

873

874 **Fig. 4.** Oxygen isotopic compositions of the entire dataset of chondrule olivine crystals from
875 the LL3 Bishunpur, Piancaldoli, and Semarkona chondrites. The data highlight important
876 mass-independent variations (up to 50 ‰), defining a good correlation: $\delta^{17}\text{O} = [0.97 \pm 0.02]$
877 $\times \delta^{18}\text{O} - [1.0 \pm 0.9] \text{‰}$ (MSWD = 4.7, $r^2 = 0.94$, $n = 649$). Relict olivine grains ($n = 17$; following
878 the definition of Ushikubo et al., 2012) have variable O isotopic compositions. Host grains
879 define a correlation of $\delta^{17}\text{O} = [0.76 \pm 0.06] \times \delta^{18}\text{O} - [0.08 \pm 0.14] \text{‰}$ (MSWD = 0.21, $r^2 = 0.80$,
880 $n = 632$) and are characterized by a slope shallower than that of the entire dataset but
881 steeper than 0.52. The Terrestrial Fractionation Line (TFL) and Primary Chondrule Minerals
882 line (PCM; Ushikubo et al., 2012) are shown for reference.

883

884 **Fig. 5.** (A) Oxygen isotopic composition of olivine grains in chondrule Ch-6 from LL3.15
885 Bishunpur. All olivine grains in this chondrule correspond to host olivines, with relatively
886 constant $\Delta^{17}\text{O} = 0.9 \pm 0.8 \text{‰}$ but variable $\delta^{18}\text{O}$ values from 0.9 to 6.4 ‰. This defines a good
887 correlation with $\delta^{17}\text{O} = [0.52 \pm 0.06] \times \delta^{18}\text{O} + [0.9 \pm 0.2] \text{‰}$ (MSWD = 1.70, $r^2 = 0.75$, $n = 65$),
888 revealing important mass-dependent fractionation within this chondrule. (B) Oxygen isotopic
889 composition of olivine grains in chondrule Ch-6 from LL3.10 Piancaldoli. This chondrule
890 contains seven relicts with variable ^{16}O enrichments. Host grains define a good correlation
891 with $\delta^{17}\text{O} = [1.00 \pm 0.11] \times \delta^{18}\text{O} - [1.7 \pm 0.6] \text{‰}$ (MSWD = 2.52, $r^2 = 0.73$, $n = 50$). This trend
892 indicates that the host grains follow the mass-independent fractionation trend of the relicts,
893 thus emphasizing the respective roles of gas-melt interactions and the recycling of refractory
894 inclusions.

895

896 **Fig. 6.** Gray-scale high-resolution TiO₂ X-ray maps of chondrules (A) Ch-1 from Bishunpur and
897 (B) Ch-25 from Piancaldoli. TiO₂ concentration increase from black to white. The O isotopic
898 compositions ($\delta^{18}\text{O}$) of olivine grains are overlain (color scale). Olivines in the inner and
899 outer parts of the chondrules tend to have isotopically heavier and lighter compositions,
900 respectively. Isotopic zonings are also observed at the grain scale (see section 4.2 for
901 details).

902

903 **Fig. 7.** $\Delta^{17}\text{O}$ values as functions of incompatible element concentrations: (A) TiO₂, (B) Al₂O₃,
904 (C) CaO, (D) MnO, and (E) NiO. ¹⁶O-poor host olivine grains exhibit variable minor element
905 compositions, whereas ¹⁶O-rich relict grains define two distinct groups: (i) those with
906 extreme ¹⁶O enrichments ($\Delta^{17}\text{O} < -15\text{‰}$) are systematically Al- and Ti-poor, whereas others
907 (ii) with $\Delta^{17}\text{O} \approx -5.5\text{‰}$ show variable minor element abundances. (F) Mg# vs. $\Delta^{17}\text{O}$ values. In
908 all plots, the black line and gray rectangle define the average $\Delta^{17}\text{O}$ value and 2 SD range,
909 respectively, for all host olivine grains. ($\Delta^{17}\text{O}$ vs. Cr₂O₃ is shown in Fig. S12).

910

911 **Fig. 8.** $\Delta^{18}\text{O}$ vs. $\Delta^{17}\text{O}$ diagram for host and relict chondrule olivine grains from OCs (red) and
912 CCs (blue). The $\Delta^{18}\text{O}$ and $\Delta^{17}\text{O}$ values of host olivines (squares) correspond to average values
913 for each individual chondrule, whereas those of relict olivines represent measurements of
914 individual grains (circles). The mean host chondrule values and 1 SD ranges are represented
915 as solid-colored lines and colored rectangles, respectively (OCs, $1.1 \pm 0.5\text{‰}$; CCs, 3.4 ± 0.5
916 ‰ ; 1 SD). The colored dashed-dotted lines represent the mean OC and CC host chondrule
917 compositions along lines parallel to the PCM (black dashed-dotted line). O-isotopic
918 compositions of olivine grains in AOAs are shown for comparison. The TFL and PCM are
919 shown for reference; the black solid PCM line shows a constant $\Delta^{18}\text{O} = 2.7\text{‰}$, whereas the

920 black dashed-dotted line is the true PCM. Errors on $\Delta^{18}\text{O}$ are 2 SD whereas those on $\Delta^{17}\text{O}$ are
921 2 SE. CC data, for the C2-ung NWA 5958 and the CV3 Kaba, are from Marrocchi et al. (2018,
922 2019a), respectively. Oxygen isotopic data of Kaba (CV3.1) and DOM 08006 (CO3.05) AOAs
923 are from Krot et al. (2019); Marrocchi et al. (2019b) and Fukuda et al. (2021).

924

925 **Fig. 9.** Schematic representation of gas-melt interactions during the OC chondrule-forming
926 events. Upon heating, the partial melting of proto-chondrules removed any evidence of
927 early isotopic disequilibrium within the melt. Chemical disequilibrium between the melts
928 and the undersaturated gas caused the evaporation of isotopically light gas, forming
929 isotopically heavy chondrule melts. Upon cooling, the condensation of the isotopically light
930 gas onto the chondrules progressively enriched the chondrule melts in light O isotopes. The
931 subsequent fractionated crystallization of olivine grains, either as overgrowths on relict
932 olivines or as new grains, preserved the successive O isotopic compositions of the melt. Host
933 olivine grains thus record the O isotopic evolution of the melt from heavy to lighter
934 compositions. We note that the true extent of the mass-dependent O isotopic fractionation
935 depends on the exact thermal history. See section 4.2 for further details.

936

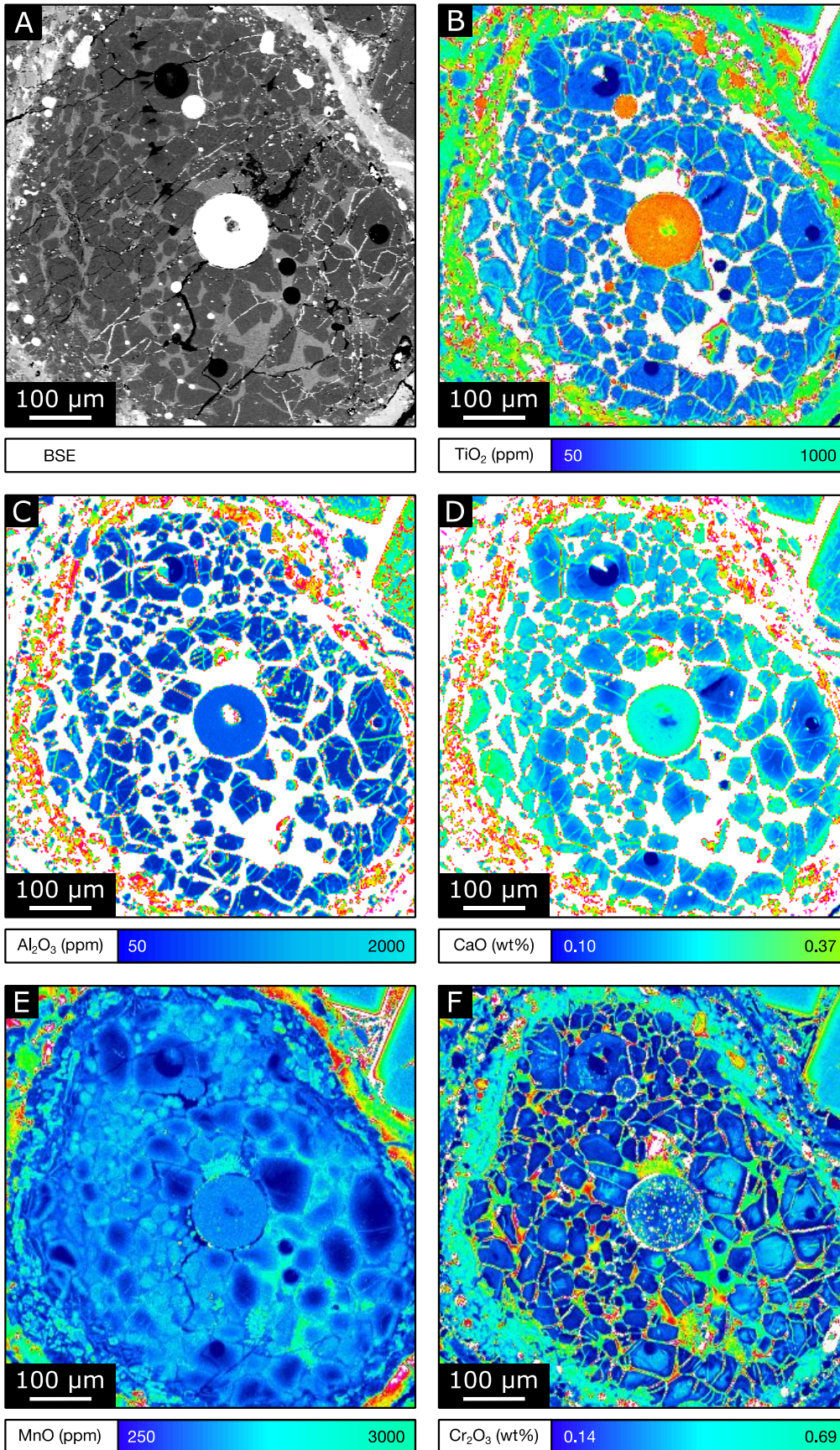
937 **Fig. 10.** $\Delta^{18}\text{O}$ vs. $\Delta^{17}\text{O}$ diagram of (A) the average O isotopic compositions of host olivine
938 grains and (B) the O isotopic compositions of bulk chondrules for OCs (diamonds) and CCs
939 (circles), represented as a function of the modal abundance of chondrules in each chondrite
940 (color scale). The solid gray line represents the PCM at a constant $\Delta^{18}\text{O} = 2.7\text{‰}$, whereas the
941 dashed-dotted line is the true PCM line. In (A), errors on $\Delta^{18}\text{O}$ are 2 SD and those on $\Delta^{17}\text{O}$ are
942 2 SE; average host O isotopic compositions are from this study and Kita et al. (2010),
943 Chaumard et al. (2018), Hertwig et al. (2018), Marrocchi et al. (2018, 2019a), Schneider et al.

944 (2020), and Williams et al. (2020). In (B), errors on $\Delta^{18}\text{O}$ and $\Delta^{17}\text{O}$, when given, are smaller
945 than the symbol size; bulk chondrule O isotopic compositions are from Clayton et al. (1983,
946 1991), Clayton and Mayeda (1985, 1999), Mayeda et al. (1988), Rubin et al. (1990), Weisberg
947 et al. (1993), and Jones et al. (2004). Chondrule fractions in the different chondrite groups
948 are from Scott and Krot (2014) and normalized to 100 %.

949

950 **Fig. 11.** Schematic representation of OC chondrule formation. Early-condensed ^{16}O -rich AOA-
951 like dust was recycled through partial melting and gas-melt interactions. This included (i) the
952 melting of AOA-inherited Ti-Al-rich components, (ii) the partial dissolution of ^{16}O -rich relict
953 olivine grains (orange), and (iii) the crystallization of Ti-Al-rich and ^{16}O -poor host olivine
954 (blue). Later recycling of earlier OC chondrule generations occurred following the same
955 processes. The partial melting of previous generations of olivine grains, including both relict
956 and host grains, and interactions with a relatively ^{16}O -poor gas created different types of
957 relicts (Relicts #1 inherited from AOA-like dust in orange, and Relicts #2 inherited from early
958 chondrule host olivine in blue) and newly crystallized ^{16}O -poor host olivine grains (black).
959 See section 4.3 for further details.

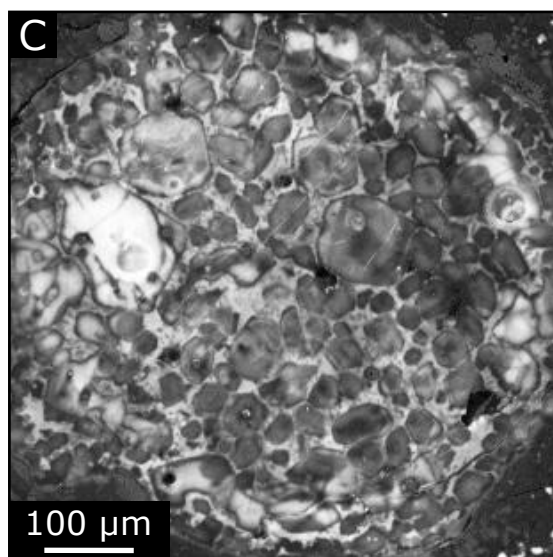
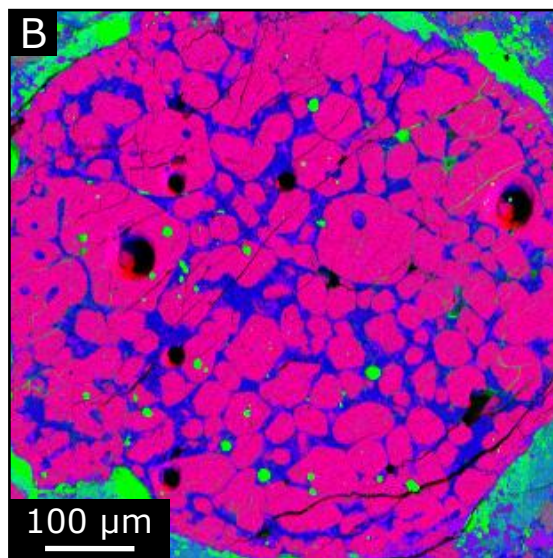
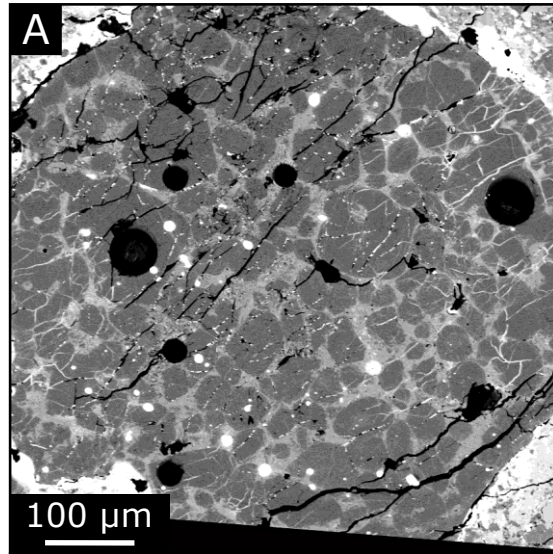
960



961

962

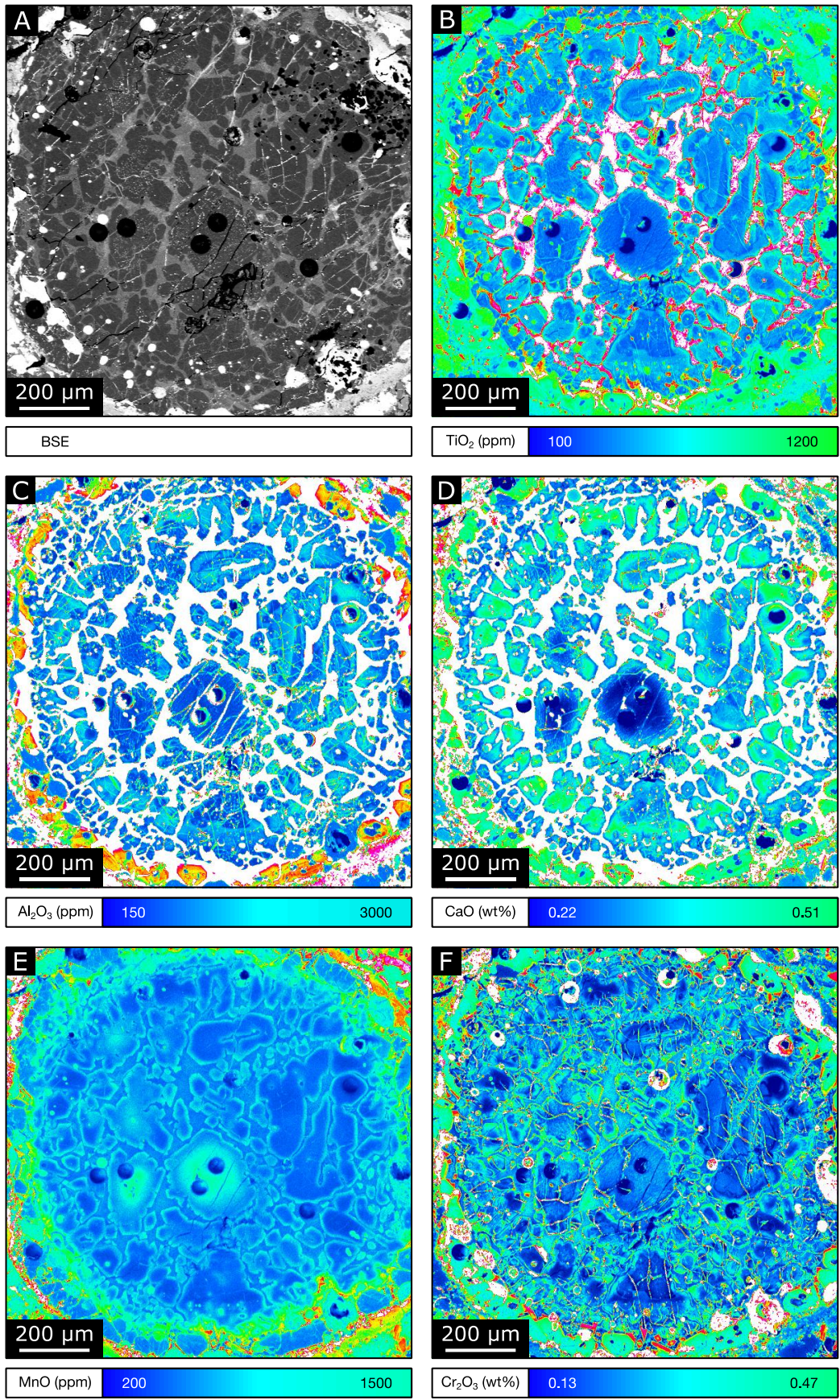
Fig. 1



963

964

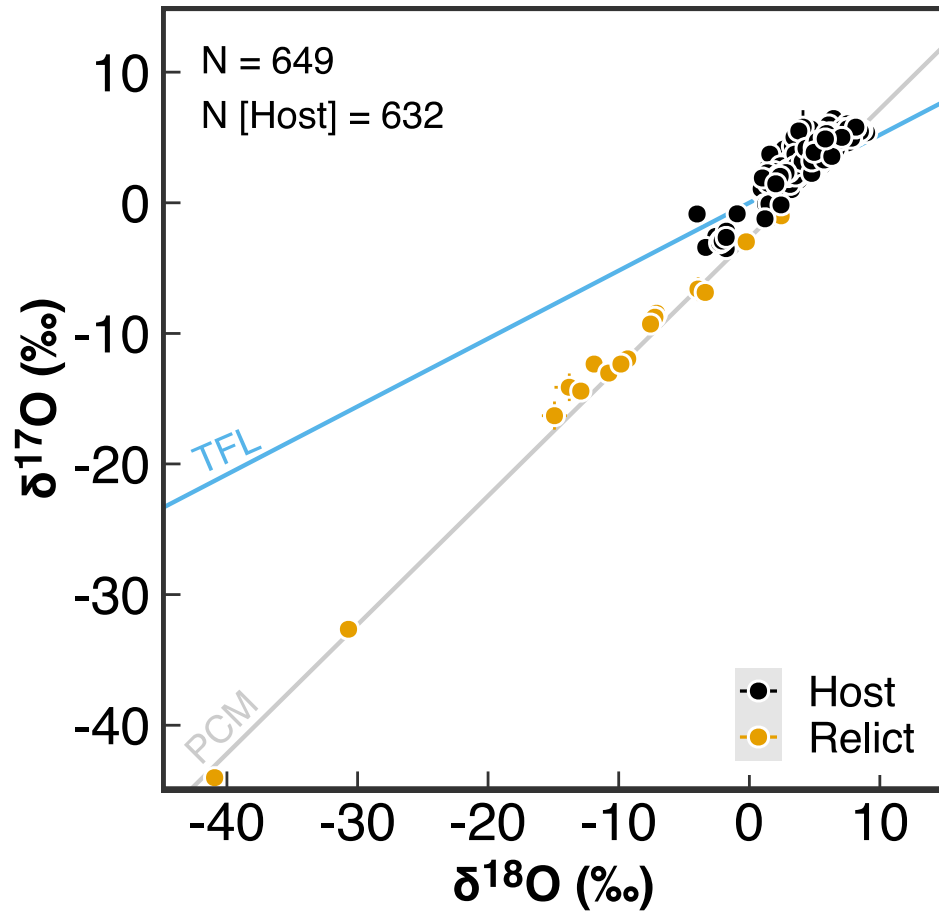
Fig. 2



965

966

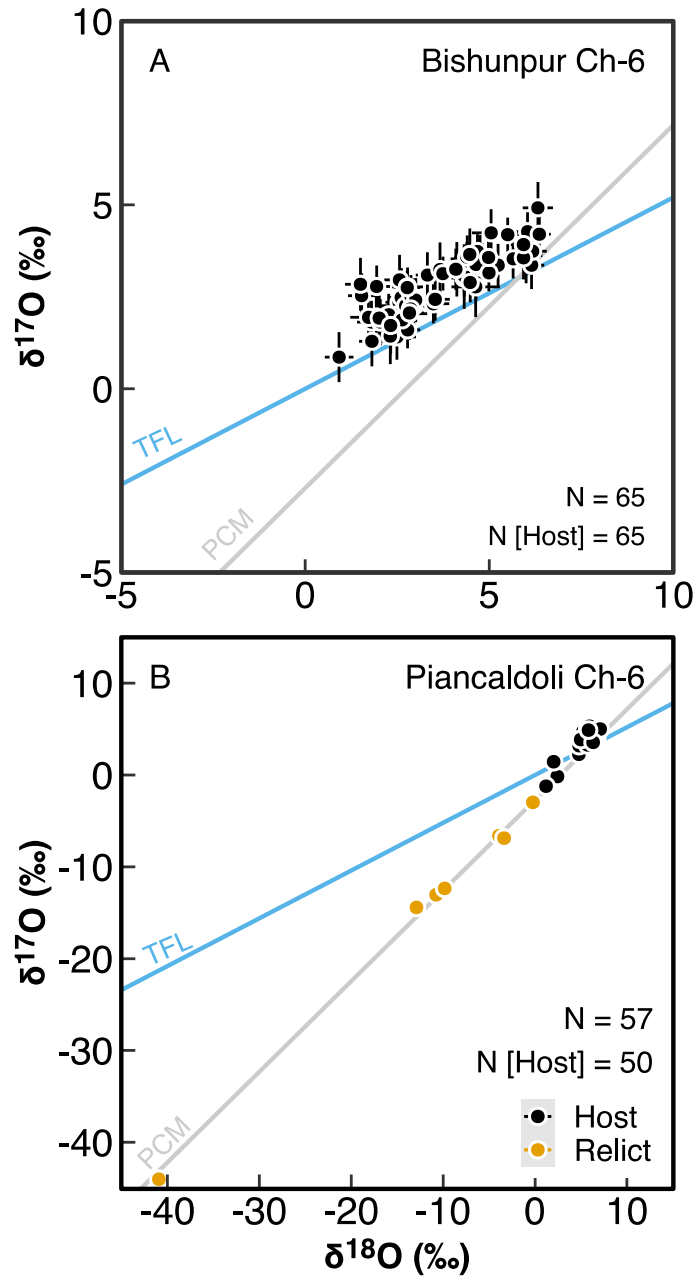
Fig. 3



967

968

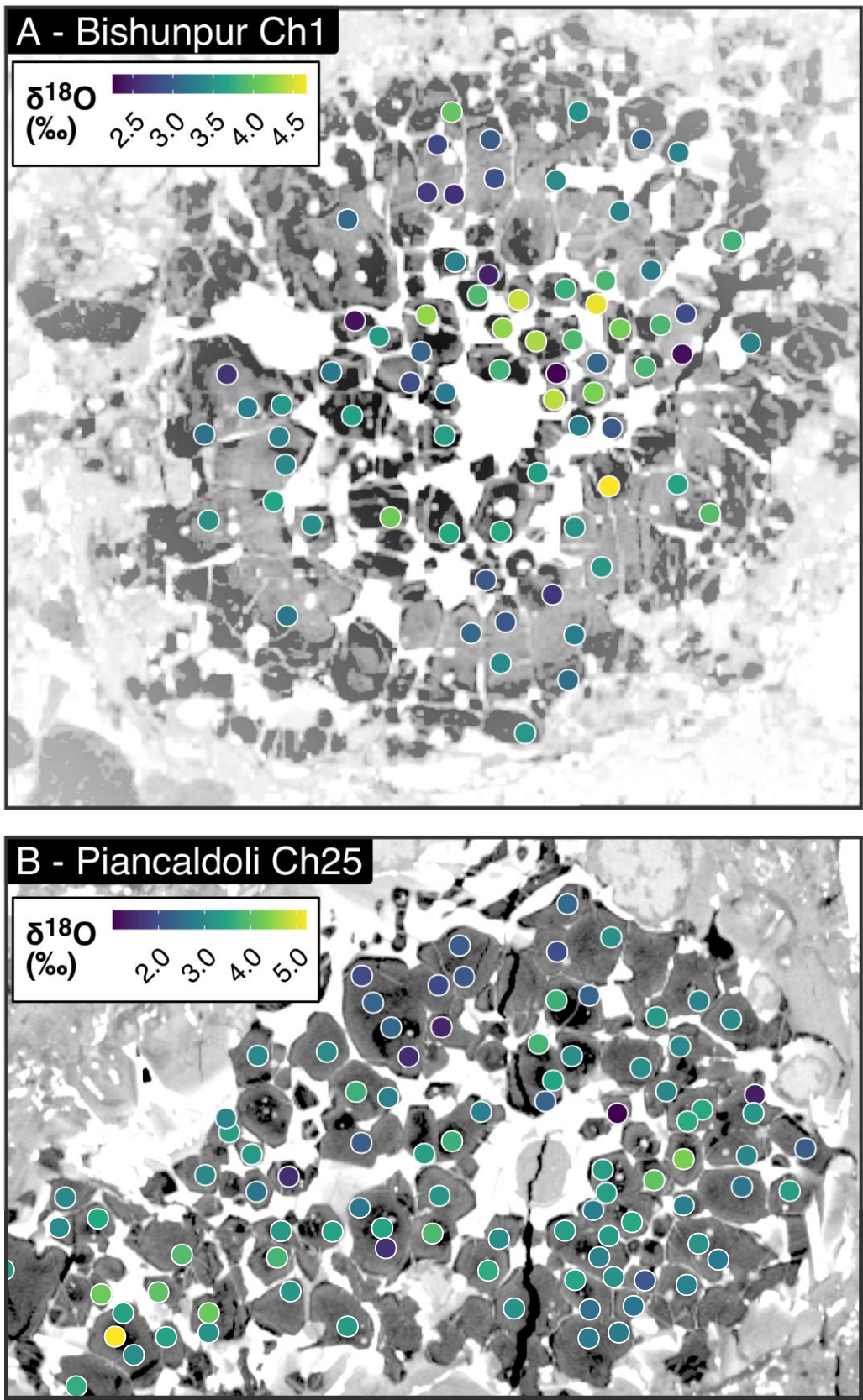
Fig. 4



969

970

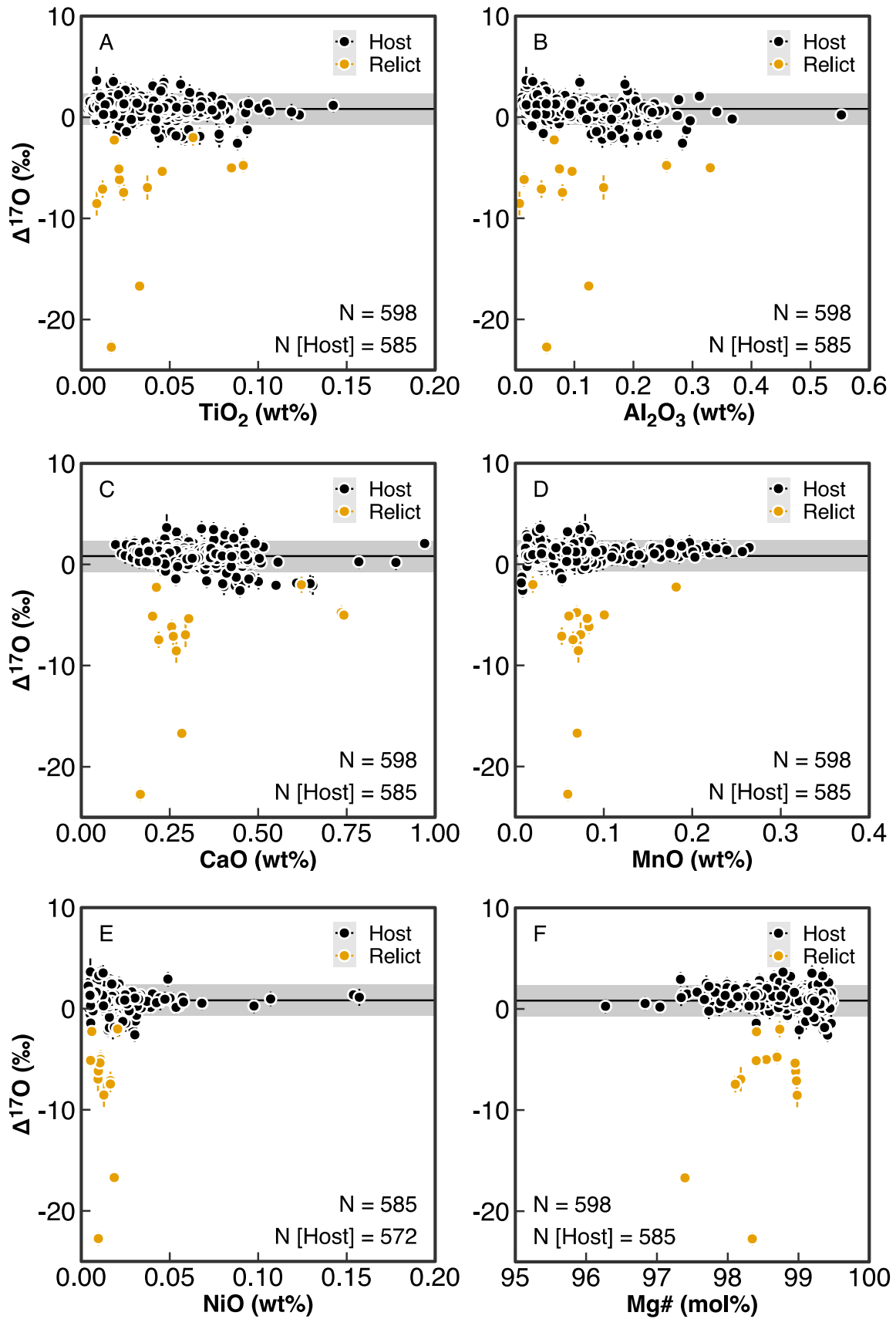
Fig. 5



971

972

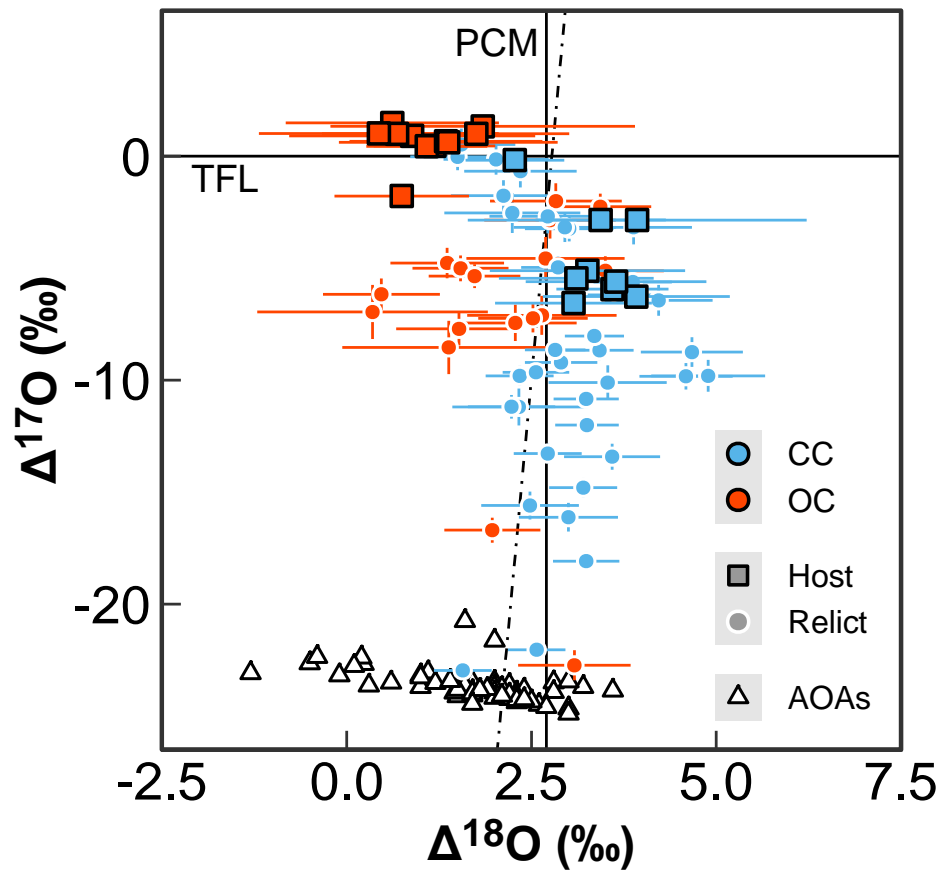
Fig. 6



973

974

Fig. 7

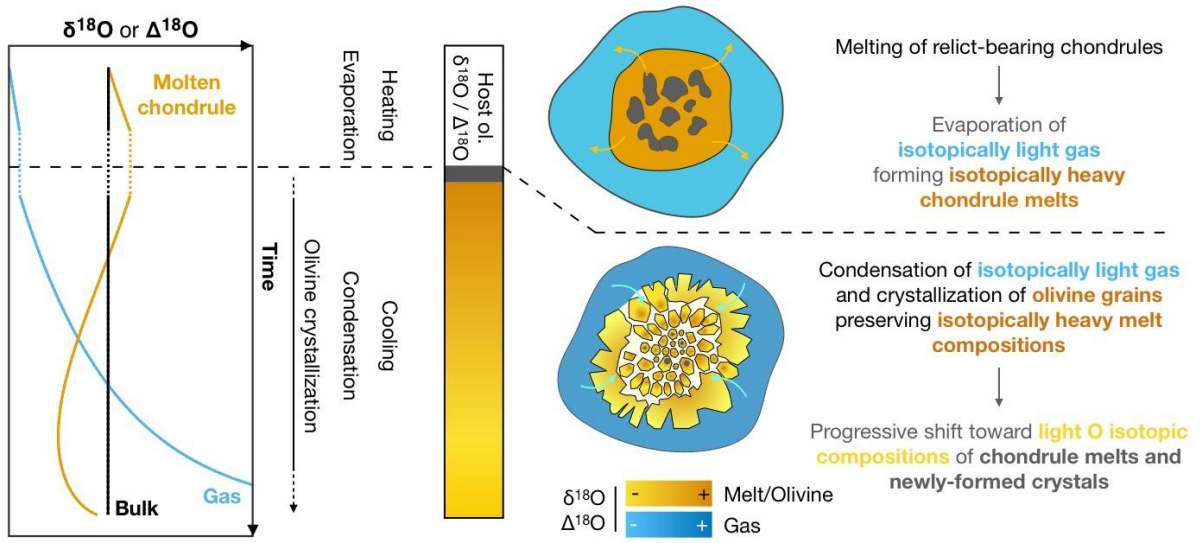


975

976

977

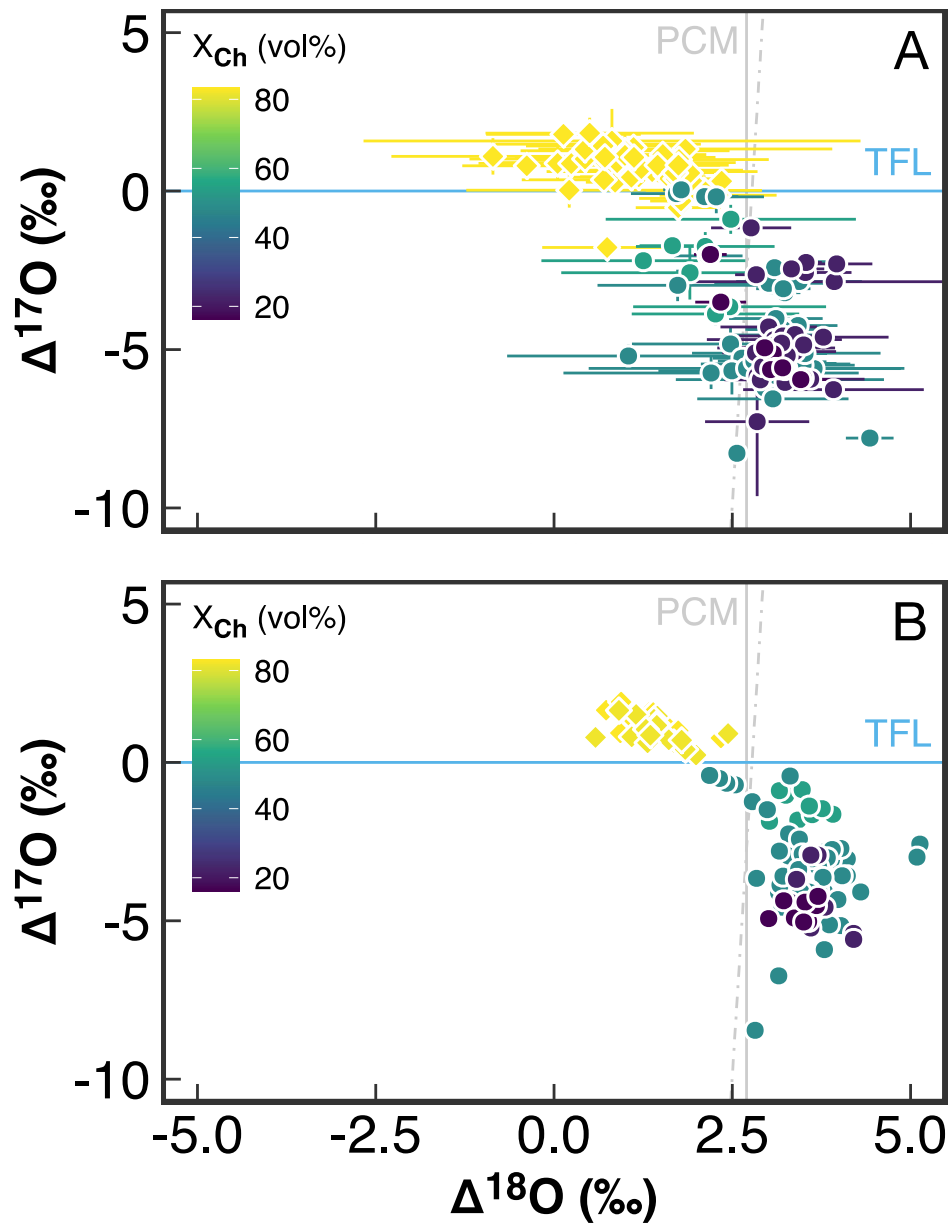
Fig. 8



978

979

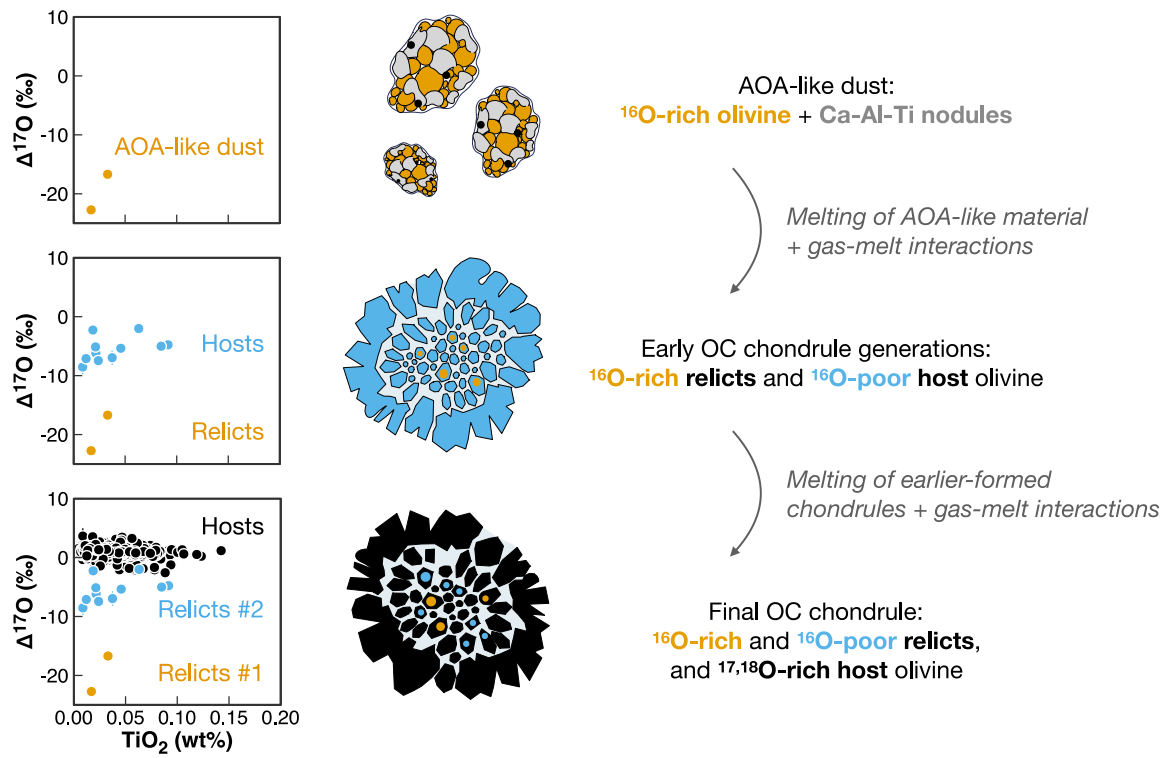
Fig 9



980

981

Fig. 10



982

983

Fig. 11